energies

MDPI

Article

The Influence of the TiO_2 Compact Layer on the Performance of Carbon-Based Ambient-Synthesized $CH_3NH_3PbI_3$ Solar Cells

Cheikh Zakaria Eldjilali [1], Pei-Ling Low [1,2], Gregory Soon How Thien [2], Yew-Keong Sin [1,2], Boon Kar Yap [3,4,5], Kar Ban Tan [6] and Kah-Yoong Chan [1,2,*]

[1] Faculty of Artificial Intelligence and Engineering, Multimedia University, Persiaran Multimedia, Cyberjaya 63100, Selangor, Malaysia; zakaria.eldjilali@hotmail.com (C.Z.E.); pllow@mmu.edu.my (P.-L.L.); yksin@mmu.edu.my (Y.-K.S.)
[2] Centre for Advanced Devices and Systems, Centre of Excellence for Robotics and Sensing Technologies, Multimedia University, Persiaran Multimedia, Cyberjaya 63100, Selangor, Malaysia; gregory@mmu.edu.my
[3] Electronic and Communications Department, College of Engineering, University Tenaga Nasional, Kajang 43000, Selangor, Malaysia; kbyap@uniten.edu.my
[4] Institute of Sustainable Energy, University Tenaga Nasional, Kajang 43000, Selangor, Malaysia
[5] International School of Advanced Materials, South China University of Technology, 381 Wushan Road, Tianhe District, Guangzhou 510006, China
[6] Department of Chemistry, Faculty of Science, Universiti Putra Malaysia, Serdang 43400, Selangor, Malaysia; tankarban@upm.edu.my
* Correspondence: kychan@mmu.edu.my

Abstract

Since their discovery in 2009, perovskite solar cells (PSCs) have demonstrated rapid progress. Ambient-processed, carbon-based PSCs utilizing a pre-heating step offer a cost-effective fabrication route. Nevertheless, the role of the compact titanium dioxide (TiO_2-c) layer in ambient conditions has remained under-explored and inconsistently reported in the literature. This study then investigated the impact of TiO_2-c layer thickness, ranging from 70 nm to 155 nm, on the performance of PSCs fabricated entirely in ambient air with high relative humidity (RH > 70%). The layers were deposited via the sol-gel spin-coating method. Experimental results then revealed that the thinnest layer (70 nm) yielded the lowest average power conversion efficiency (PCE) of 2.05% due to diminished J_{sc} and V_{oc} values. The optimized TiO_2-c thickness was also identified at 95 nm, achieving an average PCE of 2.95% and a peak efficiency of 4.5%. Structural analysis via XRD confirmed the presence of both anatase and brookite phases. Notably, increasing the thickness from 70 nm to 155 nm resulted in a slight reduction in the anatase peak and a corresponding increase in the brookite peak. The superior performance at 95 nm could be attributed to a balanced crystal intensity between these two phases. Furthermore, TiO_2-c thickness was found to correlate with larger aggregate formation, better uniform shape grains, and reduced surface roughness, significantly influencing the morphology of the subsequent mesoporous TiO_2-m layer. These findings then provided critical insights into how thickness variation in the TiO_2-c layer could influence the performance of ambient-processed carbon-based PSCs.

Keywords: TiO_2-c effect; perovskite solar cells; carbon-based solar cells; C-PSCs; electron transport layer effect

Academic Editors: Arnold Johan Rix and Alan Brent

Received: 21 February 2026
Revised: 9 April 2026
Accepted: 10 April 2026
Published: 17 April 2026

1. Introduction

The amount of energy that reaches the surface of Earth from solar irradiation each second is approximated to be 1.08×10^{14} kW [1,2]. Notably, the abundance of solar energy

places significant attention on exploiting solar cell technologies as a form of renewable energy. In 2022, solar power constituted 31% of the total renewable energy installed [3]. While monocrystalline and polycrystalline silicon solar cells are the leading commercially used solar technologies, their material and energy-intensive production hinders their worldwide adoption [4,5]. Organic photovoltaic [6], dye-sensitized solar cells [7,8], and quantum dot solar cells [9] are among the technologies that gained some research interest in the past few decades.

Perovskite solar cells (PSCs) are one of the newest emerging technologies that gained a big interest in the research community due to their unmatched rapid progress in power conversion efficiencies (PCE) from 3% in 2009 to over 26% in 2024 [10,11]. Low cost of the resource materials, low-energy fabrication processes, and the wide absorption wavelength that ranges between 400 nm and 750 nm, with some perovskites reaching the 1100 nm range, are among the reasons that set perovskite technology ahead of its competitors [12,13].

A perovskite layer is typically sandwiched between an electron transport layer (ETL) and a hole transport layer (HTL). A transparent conductive layer (TCO) is used as the front electrode, while either a metal or carbon-based material is used as the back electrode. Some commonly used ETL materials include titanium dioxide (TiO_2) [14], tin oxide (SnO_2) [15], zinc oxide (ZnO) [16], niobium oxide, and (6,6) phenyl-C_{61}-butyric acid methyl ester (PCBM) [17]. Meanwhile, HTL materials that have been investigated are 2,2′,7,7′-tetrakis(N,N-di-p-methoxyphenylamine)-9,9′-spirobifluorene (Spiro-OMeTAD) [18], poly[bis(4-phenyl)(2,4,6-trimethylphenyl)amine] (PTAA) [19], copper thiocyanate (CuSCN) [20], poly(3-hexylthiophene) (P3HT) [21], copper Iodide (CuI) [22], vanadium oxide (V_2O_5) [23], and nickel oxide (NiO) [24].

The difference between a planar (n-i-p) structure and the inverted structure (p-i-n) lies in the placement of the ETLs and HTLs in the PSC device. In an n-i-p structure, the ETL is deposited above the TCO and below the perovskite layer, followed by the HTL and the back electrode. On the other hand, an inverted p-i-n structure places the HTL above the TCO, and the ETL below the back electrode. The consideration of using n-i-p or p-i-n structure depends on the materials and the techniques used in the fabrication of the PSC device. For example, the high-temperature requirement (200 to 400 °C) for the annealing of titanium dioxide (TiO_2) makes it a suitable ETL material for n-i-p structure only. If used in an inverted structure, it can lead to degradation and destruction of the perovskite layer.

Metal-based back electrode perovskite solar cells (M-PSCs) are among the most investigated types, with the highest reported PCEs using gold (Au) [11,25,26] for (n-i-p) structure or silver (Ag) [27,28], aluminum (Al), or copper (Cu) [29] for inverted structured. Generally, metal electrodes are deposited using thermal evaporation, requiring high vacuum conditions, which consecutively reduces their potential for commercial use [30]. Likewise, carbon-based back electrode perovskite solar cells (C-PSCs) are more favorable due to the lower production cost associated with the use of carbon as an electrode and the low energy consumption of the deposition techniques employed, such as doctor blading [31,32], inkjet printing [33], and screen printing [34].

The research community primarily utilizes two distinct types of C-PSCs, differentiated by their structure and fabrication. Mesoporous carbon-based PSCs feature a multi-layered architecture of compact TiO_2, mesoporous TiO_2, mesoporous zirconium dioxide ZrO_2, and a carbon layer (TiO_2-c/TiO_2-m/ZrO_2-m/carbon). Due to the high annealing temperature of 500 °C required for these layers, the perovskite solution must be infiltrated (drop cast) from the carbon side after annealing [30]. In contrast, paintable carbon-based PSCs are distinguished by their use of a carbon paste that allows for low-temperature annealing (80 °C to 130 °C). Their structure resembles a planar n-i-p configuration, typically comprising the ETL, the perovskite layer, the HTL, and finally, the carbon electrode [35]. The use of an HTL

in paintable C-PSCs can increase the performance of the device; for example, a structure of FTO/TiO_2/perovskite/spiro-OMeTAD/carbon achieved a PCE of 19.2%.

The use of an HTL in paintable C-PSCs can increase the performance of the device; for example, a structure of FTO/TiO_2/perovskite/spiro-OMeTAD/carbon achieved a PCE of 19.2% [36]. On the other hand, a number of investigations have focused on HTL-free paintable C-PCSs due to their lower fabrication costs and high potential for commercial applications. This is primarily because spiro-OMeTAD—one of the most commonly used hole transport materials—is highly expensive to synthesize, with prices ranging from \$170 to \$475 per gram [37]. The cost of using a spiro-OMeTAD layer as HTL and Au as electrode has been estimated to be 33.9% and 18.39% when fabricating a 1 m^2 PSC module with the structure FTO/TiO_2/Spiro-OMeTAD/Au [38]. HTL-free structure offers a reduction in production cost and design simplification. However, the use of carbon as an electrode results in further cost savings [39]. Huiyun Wei et al. reported in 2015 HTL-free paintable C-PSCs with PCEs ranging from 10.27% to 13.53% by changing the graphite and carbon black composition ratio in the carbon layer [40]. Another HTL-free paintable C-PSC study in 2016 reported improvement from 4.47% to 6.16% in their PCEs by modifying the carbon layer composition [41]. Some of the recent studies in this field include the work by Shoaib Iqbal et al. in 2023, reporting devices with PCEs ranging between 9.65% to 14.17% by optimizing the N2 pressure used in the fabrication process [31].

While perovskite solar cells (PSCs) have achieved remarkable efficiencies, their commercial viability relies heavily on transitioning away from strict, inert-environment manufacturing. Because the perovskite crystallization process is highly vulnerable to oxygen and moisture, ambient-air fabrication remains a significant challenge. To overcome the detrimental effects of high environmental humidity, researchers have developed targeted ambient-processing strategies such as antisolvent bathing [42]. For instance, pre-heating the substrate prior to deposition has emerged as a highly effective method to control crystallization kinetics in open air. Notably, Tai et al. demonstrated that this pre-heating technique successfully mitigated moisture degradation, nearly doubling the device's power conversion efficiency (PCE) from 8.78% to 15% even under severe high-humidity conditions (RH > 70%) [43].

TiO_2 is one of the most used ETLs in planar PSCs and can be divided into two types, namely compact (TiO_2-c) or mesoporous (TiO_2-m) layers. TiO_2-c acts as a hole-blocking layer to prevent holes from reaching the electrode. The energy bandgap of a TiO_2-c layer acts as an energy barrier for holes, simultaneously reducing the energy levels the electron would need to jump from the perovskite to the electrode layer [44]. TiO_2-m is deposited above the TiO_2-c layer, and functions as a support platform for the perovskite layer. The mesoporous structure of TiO_2 allows the infiltration of the perovskite material, resulting in a rise in the contact area between TiO_2 and the perovskite material. High interfacial contact area clears the path for rapid electron extraction [45].

A compact TiO_2 layer has been deposited using different deposition techniques such as DC sputtering [46], chemical bath deposition (CBD) [47], atomic layer deposition (ALD) [48], spray pyrolysis [49,50], pulse layer deposition [51], and spin coating [52–54]. The spin coating method has been considered the preferred method for deposition by many researchers due to its minimal setup, fast deposition, and easy control that can deliver relatively precise thickness control [55].

Elaine Teixeira Veiga et al. investigated the TiO_2-c thickness effect using the layer-by-layer deposition technique with a device structure of FTO/TiO_2-c/TiO_2-m/$MAPbI_3$/spiro-OMeTAD/Au. They controlled the number of cycles from five to 30 cycles, resulting in a thickness from 9 nm to 58 nm. They also reported an extreme PSC performance dependency with thickness variation from a PCE of as low as 2.7% at 58 nm, increasing to

12% at 31 nm [56]. In a different study, TiO_2-c of 20 nm to 600 nm were investigated using spray pyrolysis for PSCs with the structure FTO/TiO_2-c/TiO_2-m/$CH_3NH_3PbI_{3-x}Clx$/spiro-OMeTAD/Ag. It was found that the best PCE was achieved at 100 nm, while at 600 nm, PCE dropped to 1.7%.

It is worth noting that PSCs with a thickness below 30 nm demonstrated volatile and weak PV performance, which they attributed to the incomplete TiO_2-c coverage [57]. Muhammad Talha M. et al. found that the optimized thickness of the TiO_2-c fabricated with the dip coating technique was 32 nm, achieving a PCE of 8.6% using PSC with the structure FTO/TiO_2-c/TiO_2-m/$MAPbI_3$/spiro-OMeTAD/Au. The range of thickness variation was between 5 nm and 50 nm. They noted that the roughness of the FTO substrate can influence the optimum TiO_2-c thickness required [44]. In a study by Huijing Liu et al., the TiO_2-c layer was fabricated using the spin coating method to study its thickness effect on PSCs with the structure FTO/TiO_2-c/TiO_2-m/$MAPbI_3$/spiro-OMeTAD/Ag. The study used variation in the volume ratio of the precursor solution to control the thickness from 15 nm to 54 nm. They found that the optimized thickness was between 26 nm and 31 nm, yielding a PCE of 12.8%, while 8.25% was recorded for the 40 nm to 50 nm range [58].

A similar study with the same PSC structure and TiO_2-c fabrication method by Weifu Sun et al. found that 152 nm was the optimized thickness, with 56 nm and 250 nm delivering lower PCEs [59]. Nevertheless, a study with a similar fabrication method for the ETLs, with a slightly different structure, compromising of TiO_2-c/$MAPbI_3$/spiro-OMeTAD/Au, examined the effect of different TiO_2-c thicknesses from 10 nm to 120 nm. A PCE of 13.59% was achieved at 19.5 nm; in comparison, further increase in the thickness to 124.2 nm led to a steep decrease in PCE to 7.29% [60]. Elshimy et al. investigated the effect of TiO_2-c layer thickness on PSCs with an FTO/TiO_2-c/$MAPbI_3$/C structure. Although they reported the number of layers rather than direct thickness measurements, they found that a six-layer configuration yielded an optimized PCE of 2.55%. Any deviation—either a higher or lower number of layers—resulted in a significant reduction in J_{sc}, V_{oc}, and FF [61].

A number of researchers have investigated the TiO_2-c thickness effect on HTL-based M-PSCs. These studies often report inconsistent optimized TiO_2-c thicknesses due to variations in deposition methods, with no consensus even among similar fabrication techniques. However, these varying reports do not indicate a lack of repeatability; rather, the ideal electron transport layer thickness is strictly dependent on the specific device architecture, the TiO_2 synthesis precursors, the deposition methods, and the perovskite materials utilized. Additionally, the deposition technique itself plays a crucial role; as Zhang et al. demonstrated, varying the TiO_2-c fabrication approach—such as utilizing CBD, sol–gel spin coating, or screen printing—yields distinctly different photovoltaic outcomes [62]. Crucially, less research has been targeted towards the TiO_2-c thickness impact in the HTL-free C-PSC structure. Thus, investigating this gap is essential, considering the huge economic and scale-up benefits offered by the HTL-free carbon-based structure.

This study focused on the impact of the TiO_2-c layer thickness for paintable HTL-free C-PSC, a device architecture that has received limited academic attention despite its potential for scalability. The TiO_2-c layer was fabricated using the sol–gel spin coating method with a PSC structure comprising glass/FTO/TiO_2-c/TiO_2-m/$MAPbI_3$/carbon, in which the whole fabrication process, including the perovskite material, was performed in ambient air with high humidity (RH > 70%) conditions. To facilitate the deposition of functioning perovskite material within this high-humidity environment, a substrate/perovskite solution pre-heating method was employed. Within this processing framework, the TiO_2-c layer thickness was systematically varied to evaluate its influence on device performance and to elucidate how the resulting morphological, optical, and structural changes correlate to the

overall photovoltaic characteristics of the PSC. Although previous studies have examined the effect of compact TiO_2 thickness across various fabrication methods, this work uniquely investigates the TiO_2-c thickness effect within an HTL-free C-PSC structure fabricated entirely in high-humidity ambient air, where the perovskite layer was specifically fabricated utilizing a pre-heating method. A PSC's architecture and its fabrication environment are critical factors that directly influence its commercialization costs. Therefore, since our chosen fabrication environment and device structure reduce the overall manufacturing costs, the results of this study can help guide future research toward lowering production expenses and advancing the commercialization of PSCs.

2. Materials and Methods

The substrate employed was fluorine-doped tin oxide (FTO)-coated glass (1.6 mm thickness, 15 Ω/sq). The chemicals and reagents employed in this experiment included Ti-nanoxide BL/SC, Ti-nanoxide T600/SC, and methylammonium iodide (MAI), all supplied by Solaronix (Aubonne, Switzerland). While lead (II) iodide (PbI_2) 99% and dimethyl sulfoxide (DMSO) anhydrous 99.9% were procured from Sigma-Aldrich (Dorset, UK/Rockville, MD, USA), dimethylformamide (DMF) was sourced from Bio Basic Canada Inc. (Markham, ON, Canada), and the DM-CAP-4703S carbon paste was acquired from Dycotec (Wiltshire, UK).

Zinc oxide (ZnO) powder and hydrochloric acid (HCL) were utilized to etch the FTO glass substrates with dimensions of 2 × 2 cm. Upon the completion of the etching process, the FTO samples were washed and cleaned in a 5-step process that included 10 min of sonication using soap, deionized (DI) water, acetone, ethanol, and one final round of DI water. Subsequently, the samples were dried in an oven (100 °C for 40 min) and using a nitrogen gun.

In order to control the TiO_2-c thickness, both the concentration and the rotation speed of the spin coater were varied. TiO_2-c solutions with 6 wt% and 3 wt% were prepared from the commercial Ti-nanoxide BL/SC solution by diluting with ethanol. In total, 5 different variations have been performed to control the thickness of the ETLs. TiO_2-c solution with 6 wt% was deposited on FTO glass using the spin coating method for 30 s, with varying the rotation speed from 2000 rpm to 4000 rpm, 6000 rpm, and 9000 rpm, while TiO_2-c with 3 wt% was spin coated only at 9000 rpm. The model used is a Specialty Coating Systems model 6808 programmable spin coater. The deposition of TiO_2-c layer and the subsequent layers was performed in ambient air with relative humidity (RT) of 70% to 85%. In the next step, the TiO_2-c sample was subjected to a 30 min annealing at 475 °C using a hotplate.

A TiO_2 mesoporous layer was deposited using the spin coating method with a 3 wt% of Ti-Nanoxide T600/SC solution. The spinning was set at 3000 rpm for 30 s, followed by the annealing of the samples at 475 °C for 30 min using a hotplate. In order to synthesize methylammonium lead iodide solution $MAPbI_3$ ($CH_3NH_3PbI_3$), 1 step deposition method was used. A mixture of 1.5 mol of MAI and PbI_2 in a DMF/DMSO solution of a 9:1 ratio was employed. In order to prepare perovskite material in an ambient air high humidity condition, the samples and the perovskite solution underwent at least 5 min pre-heating at 70 °C before the spin coating of the $MAPbI_3$ layer. The perovskite layer was deposited using spin coating at 4000 rpm for 25 s. Chlorobenzene was used as an anti-solvent solution with 1000 µL dropped at the end of 4s. Afterward, the sample was annealed at 70 °C for 1 min and 100 °C for 5 min. The doctor blade method was employed to deposit the carbon paste material, followed by a 20 min annealing on a hotplate at 100 °C. To ensure the repeatability of the study and enable the plotting of statistical distributions, a total of 32 complete PSC devices were fabricated across the five different TiO_2-c thicknesses—with at least five devices per thickness—and evaluated for their photovoltaic response.

A step profilometer model, MarSurf M400, was employed to perform the thickness measurements. For optical characterization, an ultraviolet–visible (UV–Vis) spectrophotometer model AvaSpec-ULS3648 together with a light source model AvaLight-DHC were used, sourced from Avantes (Apeldoorn, The Netherlands). In order to extract the morphology data, a Nanosurf Atomic Force Microscope (AFM) sourced from (Liestal, Switzerland) was employed. Fourier transform infrared spectroscopy (FTIR) Bruker Invenio R FM sourced from (Billerica, MA, USA) was conducted to examine the chemical compounds. The measurement area used in AFM was 10 × 10 um, with a SICON-A cantilever and EZ2-AFM heat type. Each AFM image was obtained using a 256-point/line, and a 0.5 s scanning rate per line. In order to examine the surface morphology of the samples, an FEI NanoSEM 450 field emission scanning electron microscope (FESEM) sourced from (Hillsboro, ON, USA) was utilized with a 10kV operating voltage. Electrochemical impedance spectroscopy (EIS) was recorded using a 1010E Gamry potentiostat instrument sourced from (Warminster, PA, USA). The fabricated PSCs were measured in a dark environment with a frequency range between 100 mHz and 1 MHz. The sinusoidal AC potential employed was 10 mV with a DC bias of 0.8V. For photovoltaic measurements, a Keithley series 24,000 source meter was used alongside a solar simulator model Oriel Sol2A. The standard AM1.5 100 mW/cm^2 was used in the solar measurements, and it was calibrated using a reference solar cell system model 91150V sourced from Oriel Instruments.

3. Results

3.1. Structural Properties

Figure 1 represents the thickness measurement results regarding the spin coating rotation speed and the TiO_2-c concentration. Increasing the rotation speed from 2000 rpm to 4000 rpm, 6000 rpm, and 9000 rpm resulted in a reduction in thickness from 159.3 nm to 133.25 nm, 114.28 nm, and 96 nm, respectively, for 6.0 wt% TiO_2-c concentration. Reducing the concentration to 3.0 wt% with a 9000 rpm rotation speed resulted in a further decrease of TiO_2-c thickness to 67 nm. The spin coating method permits the control of thin film thickness through changing the concentration of the solution and the rotation speed [60]. According to the Mayerhofer model, the thickness of the layer depends on many factors, such as the density and viscosity of the solution, the density of the solvent, the rate of evaporation, and the angular speed. Higher rotation speed increases the angular velocity, which is inversely proportional to the thickness of the material. Lower concentration would reduce the density of the total solution relative to the pure solvent, which will decrease the final thickness [60,63].

Figure 2a depicts the XRD pattern of the TiO_2-c (70 nm), TiO_2-c (95 nm), TiO_2-c (135 nm), and TiO_2-c (155 nm). Utilizing XRD identifies thickness-dependent changes in TiO_2-c crystallinity and phase purity that dictate electron transport characteristics. Correlating these structural properties with device data explains the impact of thickness on the overall photovoltaic performance of the PSCs.

All TiO_2-c thicknesses exhibited small overlapped peaks at 25.3 and 25.7, which correspond to the anatase and brookite TiO_2 phase with Miller indices of (101) and (111) according to ICSD Nos.: 96-720-6076 and 96-900-4140. A different small brookite peak at 31.2 can also be noticed for some TiO_2-c thicknesses. The results showcase a mixed phase for the TiO_2-c. The thinnest TiO_2-c of 70 nm exhibits a relatively larger anatase peak at 25.3 compared to the brookite peak at 25.7°. At 95 nm, the two peaks overlap, making it harder to distinguish between them. Increasing the TiO_2-c thickness to 135 nm and 155 nm results in an increase in the brookite peak intensity at 25.7° with a reduction in the 25.3 peak intensity. The current results highlight the mixed-phase crystalline structure of the compact TiO_2. The literature indicates that the XRD peaks for TiO_2 compact blocking layers typically

exhibit low intensity. This is likely attributed to the relatively small thickness required for TiO_2-c layers in perovskite solar cell (PSC) applications [44,59,64].

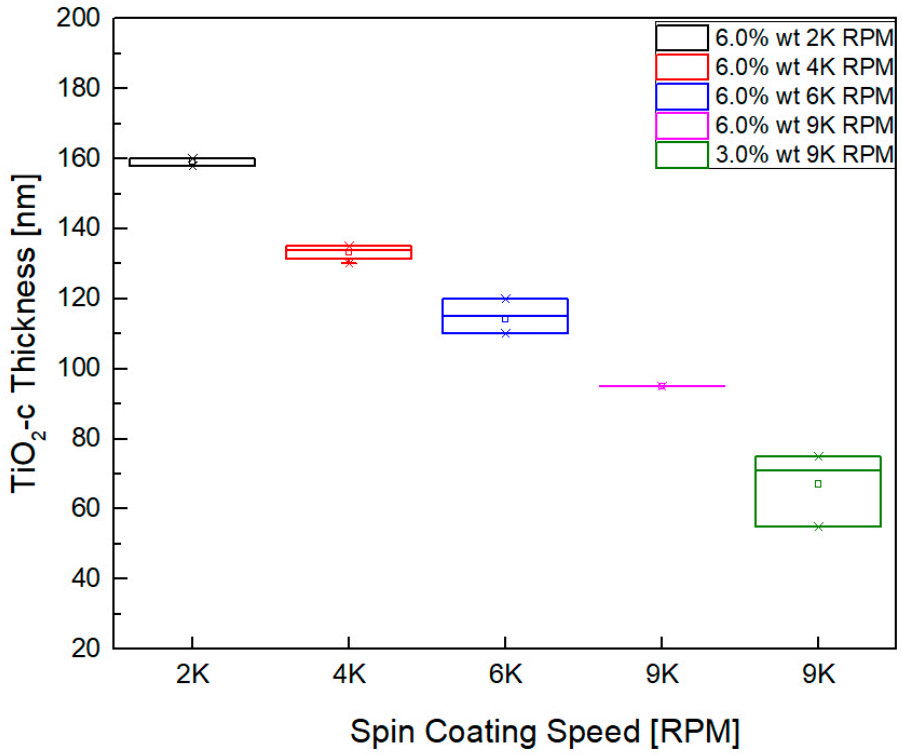

Figure 1. The impact of deposition parameters (RPM and concentration) on TiO_2-c film thickness.

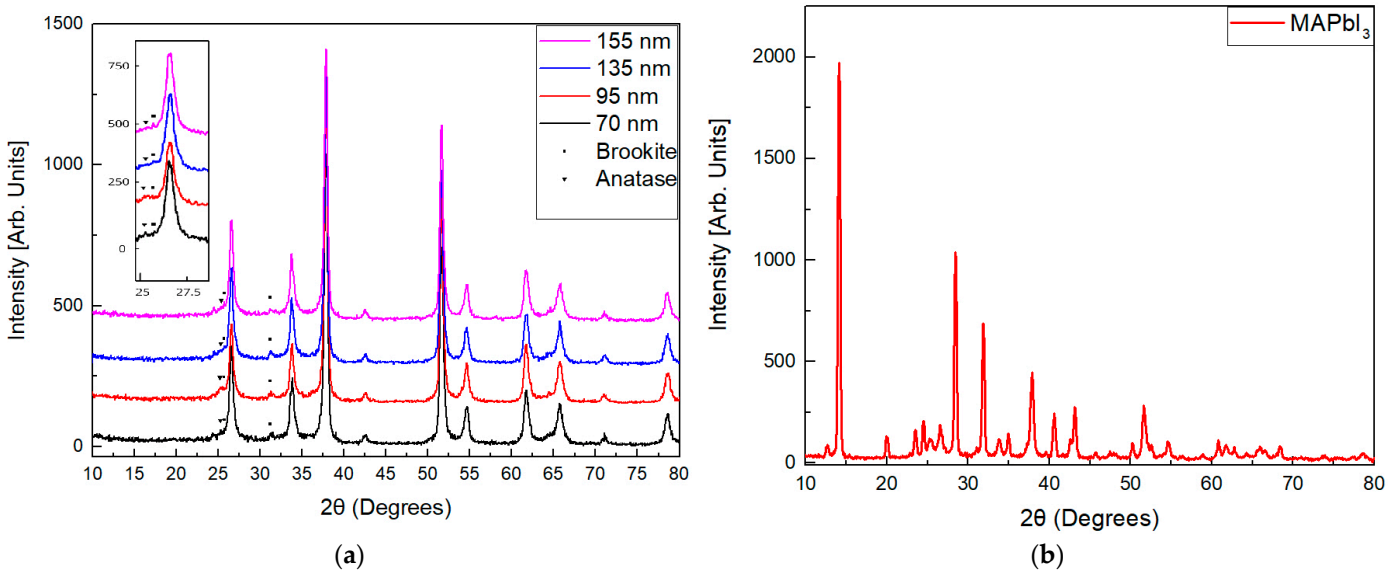

(**a**) (**b**)

Figure 2. The XRD pattern for (**a**) TiO_2-c (thickness variation deposited on FTO) and (**b**) $MAPbI_3$ deposited on FTO/TiO_2-c/TiO_2-m.

Quantitative XRD analysis using the Reference Intensity Ratio (RIR) method reveals that at a thickness of 70 nm, the TiO_2-c layer consists of a mixed phase (approx. 27 wt% anatase, 73 wt% brookite). Thicker TiO_2-c of 95 nm, 135 nm, and 155 nm resulted in further phase composition shift, where the anatase ratio is reduced to 26 wt%, 21 wt%, and 19 wt%. As the film thickness increases from 70 nm to 155 nm, the brookite phase ratio increases from 73 wt% to 81 wt%.

The anatase phase has the lowest surface energy in comparison to the brookite and rutile phases [65,66]. The critical radius required for the anatase nucleation is smaller in comparison to that of brookite [67]. Due to the thinner film thickness of 70 nm obtained by reduction in the precursor concentration and higher spin coating speed, a spatial confinement restricts the growth of the TiO_2 material, in which the nucleation is easier for the anatase grains. The higher material volume obtained by increasing the precursor concentration and reducing the spin coating speed results in slower solvent evaporation, allowing the nuclei to grow larger in comparison to the thinnest TiO_2.

The coexistence of both phases and the shift toward brookite for thicker TiO_2-c films can be explained by the size-dependent thermodynamic stability of the TiO_2 polymorphs, also known as the Zhang–Banfield crossover model [68]. The competition between surface energy and volume energy is what drives the shift in the TiO_2-c phases noticed in the XRD. Anatase is more thermodynamically preferred at small sizes because it possesses the lowest surface energy (~0.44 Jm^{-2} for anatase, 0.70 Jm^{-2} for brookite [65,66]), making it the dominant phase in the thinner TiO_2 film (75 nm), where the low precursor concentration and high spinning speed constrain the growth of the crystals. However, as film thickness increases, the higher precursor concentration and lower spin coating speed allow for grain coarsening, which pushes the crystal size past the critical thermodynamic crossover point, rendering the brookite phase energetically favorable.

Figure 2b illustrates the $MAPbI_3$ XRD pattern. The $MAPbI_3$ thin film exhibited peaks at 14.2°, 20.2°, 23.47°, 24.47°, 28.37°, 31.78°, 34.93, 40.56°, and 43.14° corresponding to the (110), (200), (221), (202), (220), (114), (312), (224), and (314) planes confirming the existence of $MAPbI_3$ material [69]. In order to calculate the crystalline size, the Debye–Scherrer formula can be used [70]:

$$D = \frac{0.9\lambda}{FWHM\ cos(\theta)} \cdots \quad (1)$$

where λ is the wavelength, *FWHM* refers to the full width at half maximum, and θ is the diffraction angle. The crystalline size at the (110) prominent peak is estimated to be 26.30 nm.

Figure 3 depicts the Fourier transform infrared spectroscopy (FTIR) for the TiO_2-c layer with a thickness of 115 nm (black color) and the $MAPbI_3$ layer (red color). FTIR was utilized to identify the characteristic vibrational modes and functional groups present on the surfaces of the TiO_2-c and $MAPbI_3$ thin films. This analysis provides experimental evidence for the formation of the Ti-O-Ti lattice and confirms the presence of the organic $CH_3NH_3^+$ components within the perovskite layer.

It is possible to observe a slope dropping starting from 400 cm^{-1} to 900 cm^{-1} with the peak observed at 825 cm^{-1}, which is evidence of the absorption from the Ti-O-Ti and Ti-O bending vibrations for the TiO_2 lattice [71,72]. A band at 3428 cm^{-1} can be observed as evidence of the stretching vibration of the O-H group [73].

The $MAPbI_3$ sample depicts an absorption peak at 669 cm^{-1} and 817 cm^{-1} correlating to the C-O and C-N stretching vibration [74]. A rocking vibration peak at 902 cm^{-1} and 966 cm^{-1} is related to $CH_3{}^-NH_3{}^+$. A high peak at 1186 cm^{-1} can be noticed, proving the existence of NH3 rocking vibrations. The IR peak at 1471 cm^{-1} is related to the $NH_3{}^-$ bending vibration. A small peak at 1575 cm^{-1} and 1635 cm^{-1} corresponds to the asymmetric $NH_3{}^-$ bending vibration of the methylammonium group [69,75].

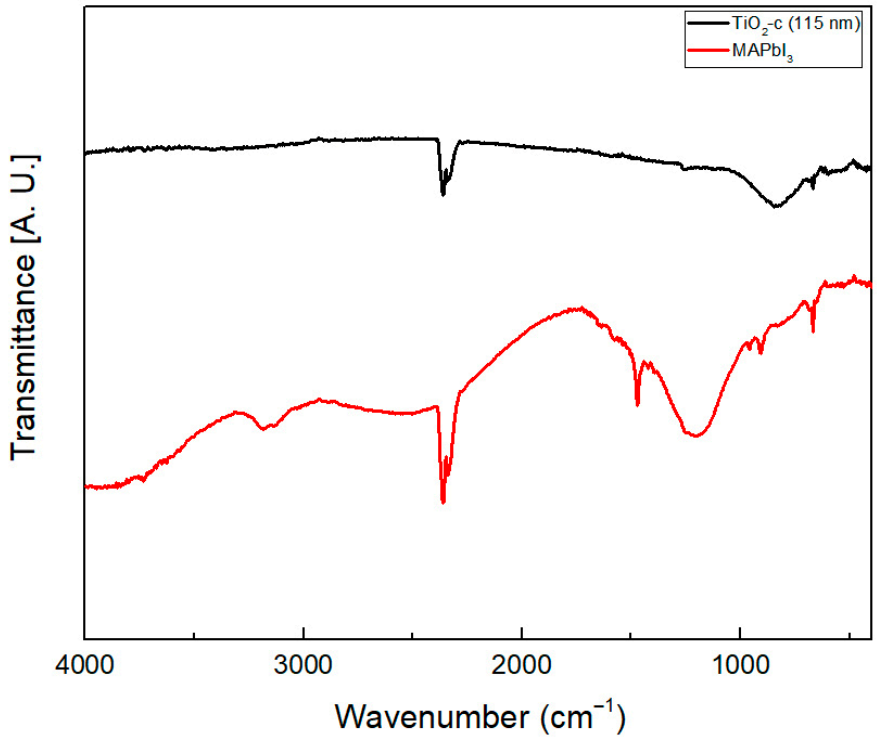

Figure 3. The FTIR pattern for TiO_2-c (115 nm) deposited on FTO (black) and $MAPbI_3$ deposited on FTO/TiO_2-c/TiO_2-m (red).

3.2. Optical Measurements

Transmittance Data

Figure 4a illustrates the transmittance spectra of the TiO_2-c layer deposited on FTO-coated glass. Characterizing the optical properties of the TiO_2-c and TiO_2-c/TiO_2-m stacks reveals how variations in the compact TiO_2 layer thickness introduce changes in overall transparency. This analysis allows for the selection of the most transparent TiO_2-c baseline, thereby increasing the amount of light that reaches the $MAPbI_3$ layer.

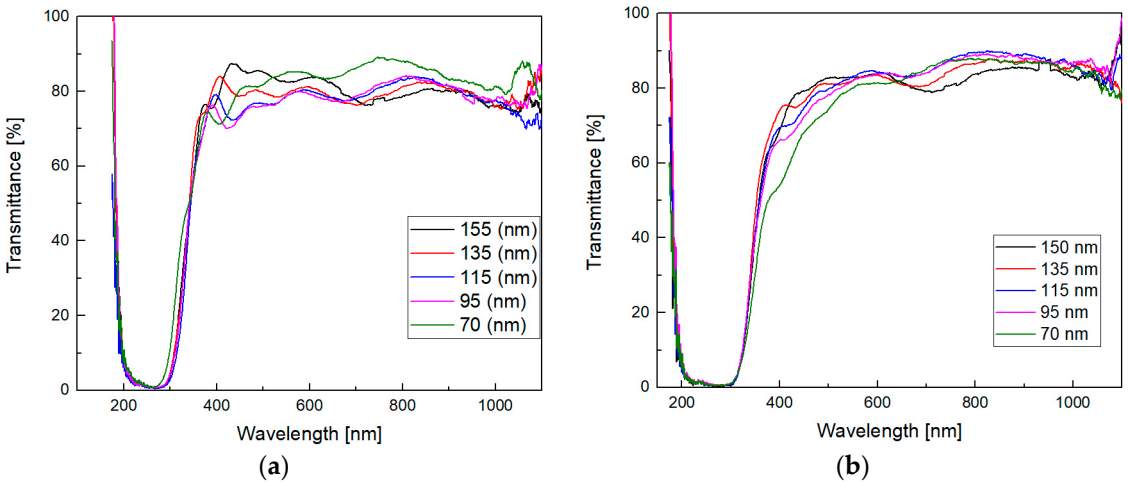

Figure 4. Transmittance spectra over the wavelength range from 150 nm to 1200 nm for (**a**) FTO/TiO_2-c (varied thicknesses), (**b**) FTO/TiO_2-c (varied thickness)/TiO_2-m deposited on TiO_2-c layer.

The TiO_2-c transmittance exhibits a transmittance range between 70% and 89% in the wavelength range from 390 nm to 1100 nm. The TiO_2-c transmittance is between 0 and 70% for the wavelength range between 200 nm and 390 nm. This is true for all TiO_2-c samples irrespective of their thickness. It is possible to observe a ripple behavior for all TiO_2-c sam-

ples. The ripple effect is a consequence of Fabry–Pérot interference [76]. As TiO_2-c thickness rises, the entire interference fringe pattern exhibits a clear red shift. While the macroscopic red shift in the transmission fringes is strictly governed by the increased optical path length in thicker films—consistent with standard Fabry–Pérot interference—the distinct red shift observed at the absorption edge is governed by a different physical mechanism. The fringe shift is a purely optical artifact of thickness; however, the absorption edge shift reflects an intrinsic microstructural evolution within the film itself. Specifically, thicker TiO_2-c films facilitate the growth of larger crystallites and subsequent larger aggregate sizes, which narrows the optical band gap and red-shifts the absorption edge [77,78]. At 750 nm, the TiO_2-c (70 nm) sample exhibits the highest transmittance of 89%, followed by 82%, 81%, 79%, and 78% for TiO_2-c thicknesses of 95 nm, 115 nm, 135 nm, and 155 nm, respectively.

Since the light-absorbing layer is deposited on the TiO_2-m layer in the solar cell structure adopted in this study, it is essential that the transmittance data, including the TiO_2-m layer, are analyzed. The transmittance of FTO/TiO_2-c (different thicknesses)/TiO_2-m is depicted in Figure 4b. The TiO_2-m deposited on TiO_2-c exhibits a similar transmittance pattern in comparison to TiO_2-c, with extremely low transmittance in the 200 nm to 380 nm region and high transmittance in the visible and near-infrared region. However, the level of the transmittance is comparably lower than that of the TiO2-c-only layer. The red shift can also be observed with a reduction in the transmittance of the previously observed ripples for TiO_2-c thickness variation. The transmittance of FTO/TiO_2-c/TiO_2-m illustrates a decreasing pattern with the increase in the thickness of the TiO_2-c layer in the visible and infrared region. At the 750 nm wavelength, the FTO/TiO_2-c (150nm)/TiO_2-m exhibit 80% transmittance, followed by 84.6%, 87.8%, 87.2%, 87.5% for 135 nm, 115 nm, 95 nm, and 70 nm TiO_2-c thicknesses.

3.3. Morphology Data

3.3.1. Atomic Force Microscopy Data

Figure 5a–e illustrates 2D Atomic Force Microscopy (AFM) images of TiO_2-c layer at varying thicknesses. It is observed that the TiO_2-c morphology consists of dense aggregates at a thickness of 70 nm. AFM characterization is essential to monitor the growth of the TiO_2 aggregates at the 10 μm scale, which provides a morphological explanation for changes in charge extraction for the TiO_2-c layer. This analysis identifies how the morphology of the transport layer dictates the resistive landscape of the PSC, directly impacting the short-circuit current and the open-circuit voltage.

Increasing the thickness from 90 nm to 135 nm is associated with larger TiO_2 aggregates, with the most significant coarsening observed in the 155 nm samples. This coarsening behavior is consistent with the growth mechanisms reported by Dundar et al., who observed that while primary crystallite sizes remain relatively stable during thickening, the physical aggregate size increases significantly (from ~40 nm to over 100 nm). This phenomenon is attributed to a Volmer–Weber 3D island growth mode, where initial nucleation islands coalesce and agglomerate into larger clusters as the deposition time and film thickness increase [77].

Figure 5f–k depicts the TiO_2-m structure deposited on the various TiO_2-c layers; the morphology of the TiO_2-m consists of larger aggregates with circular shape. TiO_2-m deposited on the 70 nm TiO_2-c reveals a uniformly distributed aggregate. Increasing the TiO_2-c thickness to 90 nm results in a comparably similar structure of uniformly distributed TiO_2-m aggregates. However, smaller aggregates can be observed. The TiO_2 mesoporous layer for the 115 nm TiO_2-c thickness manifests slightly different TiO_2 grains with irregular shapes that are less uniformly distributed. The TiO_2-m for TiO_2-c (135 nm) conveys a similar morphology to the previous thickness, with the appearance of larger grains in some spots.

The morphology of the TiO_2-m for the thickness of the TiO_2-c layer showcases a more uniform, larger TiO_2 aggregate structure.

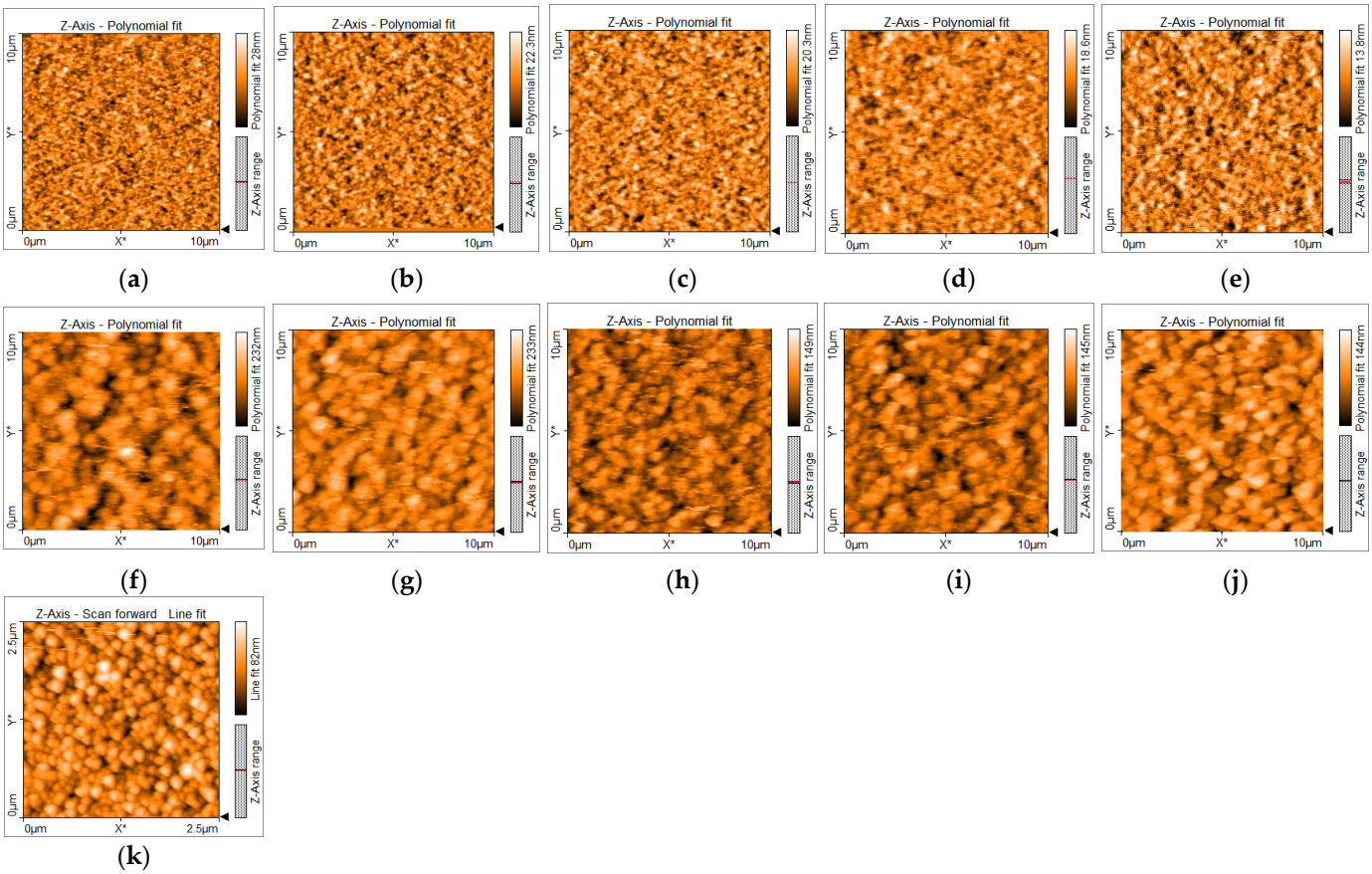

Figure 5. TiO_2-c surface Atomic Force Microscopy 2D images for (**a**) TiO_2-c thickness of 70 nm, (**b**) TiO_2-c thickness of 95 nm, (**c**) TiO_2-c thickness of 115 nm, (**d**) TiO_2-c thickness of 135 nm, and (**e**) TiO_2-c thickness of 155 nm. AFM 2D images for TiO_2-m deposited on TiO_2-c layer with different thicknesses: (**f**) TiO_2-c (70 nm)/TiO_2-m, (**g**) TiO_2-c (95 nm)/TiO_2-m, (**h**) TiO_2-c (115 nm)/TiO_2-m, (**i**) TiO_2-c (135 nm)/TiO_2-m, and (**j**) TiO_2-c (155 nm)/TiO_2-m. (**k**) AFM image of a bare FTO substrate.

Figure 6a presents the extracted TiO_2-c and TiO_2-m roughness from the AFM images. Analyzing the roughness of both TiO_2 layers reveals a structural cascade where TiO_2-c thickness dictates the smoothness of the TiO_2-m interface, a key factor in reducing trap-assisted recombination and maximizing the current density of the PSCs. The thinnest TiO_2-c highlights a roughness of 3.8 nm, followed by TiO_2-c (95 nm) with 3.64 nm. Increasing the thickness of TiO_2-c can be associated with a further decrease in roughness from 2.93 nm to 2.63 nm for 115 nm to 150 nm TiO_2-c.

A similar decreasing pattern is noticeable for TiO_2-m layer roughness. The slight change in TiO_2-c roughness is associated with a decrease in the TiO_2-m roughness. TiO_2-m deposited on the thinnest TiO_2-c layer embodies the highest roughness of 28.67 nm. Increasing the thickness of TiO_2-c further produced a decrease in the roughness of the TiO_2-m layer with a value of 26.46 nm. Further increase in the TiO_2-c thickness from 115 nm to 135 nm seems to have a more prominent decrease in the TiO_2-m roughness with 23.56 nm and 22.82 nm. However, the roughness of TiO_2-m for the thickest TiO_2-c layer is increased slightly to 23.91 nm.

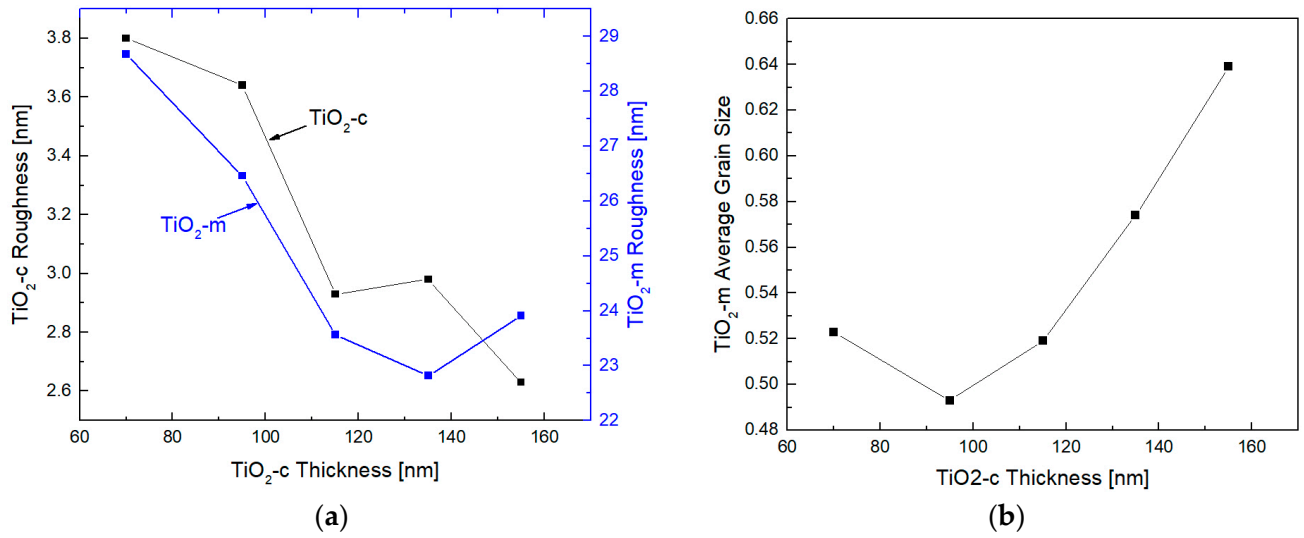

Figure 6. Extracted AFM roughness for (**a**) FTO/TiO_2-c (various thicknesses) in black, and FTO/TiO_2-c (various thicknesses)/TiO_2-m in blue; (**b**) extracted aggregate size of TiO_2-m deposited on varying TiO_2-c thicknesses.

Figure 6b depicts the TiO_2-m average aggregate size extracted from the AFM images. The average aggregate size for all samples is between 493 nm and 639 nm. The TiO_2-m deposited on the thinnest TiO_2-c layer portrays an average aggregate size of 523 nm, followed by 493 nm for the TiO_2-c (90 nm) sample. The mesoporous TiO_2 layer manifests a continuous increase in the aggregate size with the increase of TiO_2-c thickness from 90 nm to 150 nm, with an average aggregate size increasing from 493 nm to 639 nm.

Increasing the thickness of the TiO_2-c compact layer, TiO_2-c plays a dual role in the morphology and performance of perovskite solar cells. As thickness increases, the aggregate size typically grows, and the film becomes more continuous, leading to a significant reduction in surface roughness [79].

3.3.2. Field Emission Scanning Electron Microscopy Data

Figure 7a–c showcases the FESEM surface morphology of the TiO_2-c at varying thicknesses, while Figure 7d–f are the zoomed images of the varied TiO_2-c thicknesses. The TiO_2-c (70 nm) and (95 nm) depict a similar morphology, combining the existence of long TiO_2 grains that range in length between 100 nm and 250 nm, and smaller circular-shaped grains.

The likelihood of the longer TiO_2 grains appearing seems to decrease with the increase in the TiO_2-c thickness, as can be observed in the zoom-in FESEM image for the 70 to 155 nm TiO_2-c sample. The existence of both long-shaped and circular-shaped grains suggests that as the TiO_2-c layer thickness increases, a well-crystallized continuous bulk network of circular-shaped TiO_2 grains is formed. The thin TiO_2-c layer is characterized by a non-continuous network that is filled with a mixture of different-sized and shaped TiO_2 grains.

In terms of grain size, the thinnest TiO_2-c has the smallest average size of 60.28 nm, followed by the 95 nm and 155 nm TiO_2-c thicknesses with average sizes of 61.2 nm and 70.3 nm. The TiO_2-c grain distribution is more uniform in size and shape at the thickest sample, while it is extremely non-uniform at the thinnest sample.

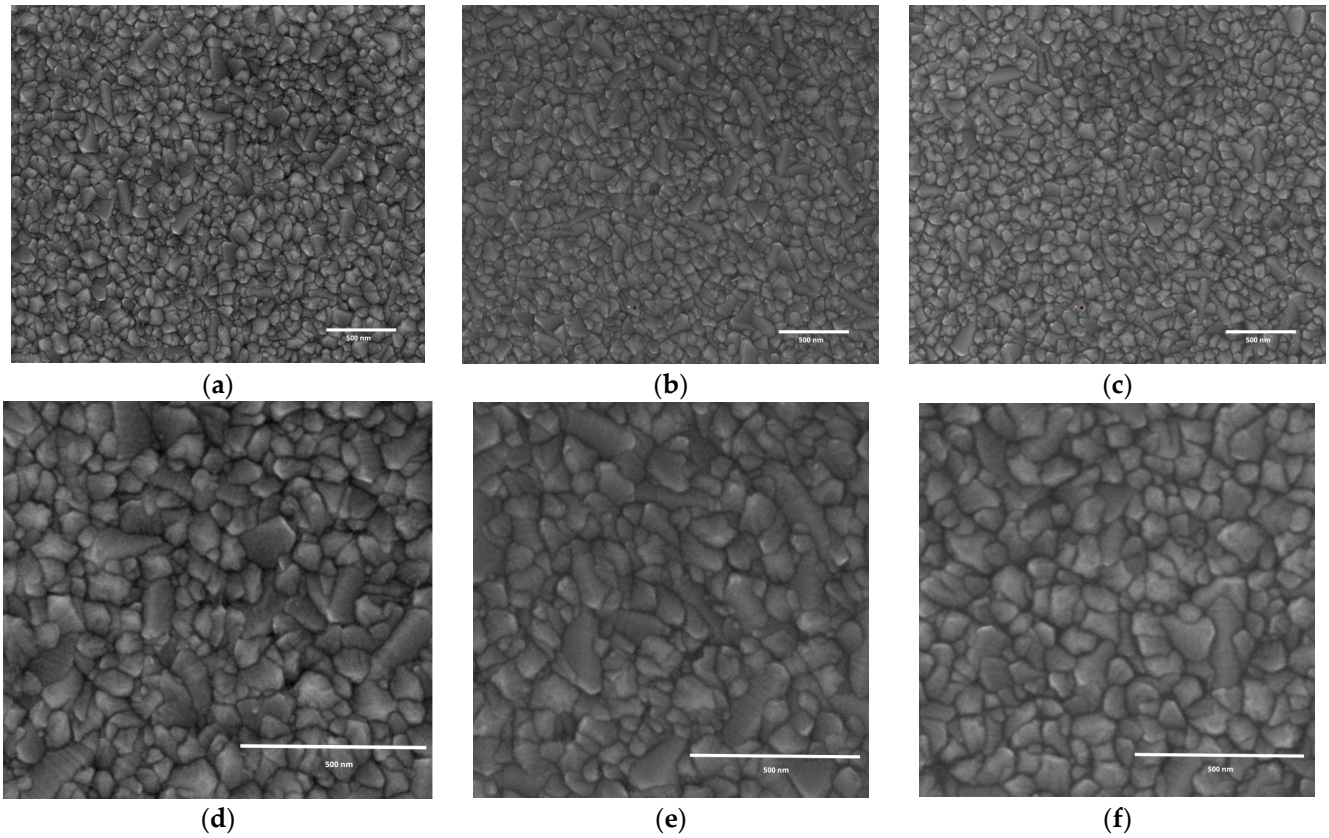

Figure 7. FESEM images for the TiO_2-c layer at different thicknesses: (**a**) TiO_2-c (70 nm), (**b**) TiO_2-c (95 nm), (**c**) TiO_2-c (155 nm). (**d**–**f**) represent the zoom in FESEM picture for the 70 nm, 95 nm, and 155 nm samples.

3.4. Charge Transport and Recombination Kinetics

Electrochemical impedance spectroscopy (EIS) characterization has been performed in dark measurements at a 0.8V bias for frequencies between 1 MHz and 100 mHz.

The Nyquist plot and the fitted plot for the 70 nm, 95 nm, and 155 nm samples are shown in Figure 8. All samples are characterized by two frequency arcs, with a positive high-frequency semicircle and a negative low-frequency semicircle. The shape showcased in this paper is similar to that reported in previous studies, and it has been labeled as the elephant feature by Will Clarke et al., showcasing a negative capacitance behavior at the low-frequency range [80]. According to Neupane et al., the negative capacitance is due to recombination due to trap states in PSCs [81], while Khan et al. attributed it to the discharge of accumulated charge to the defect states.

The apparent observation is that the high-frequency arc resistance increases as the TiO_2-c thickness decreases. This means increased thickness is associated with increased interfacial charge-transfer/charge-transport resistance.

The low-frequency semicircle is reducing with increasing TiO_2-c thickness. This means a higher thickness promotes more charge recombination.

An equivalent circuit has been used to fit the measured impedance data. The equivalent circuit that is used for the fitting was reported by Francisco et al., and it is defined as $R_s + (C_1 || (R_1 + (C_2 || L || R_2)))$, where R_1C_1 is related to the HF semicircle, while the R_2C_2 is related to the LF arc [82]. R_1 is the resistance that can be attributed to charge transfer resistance at ETL/perovskite interfaces. R_2 is attributed to recombinant resistance.

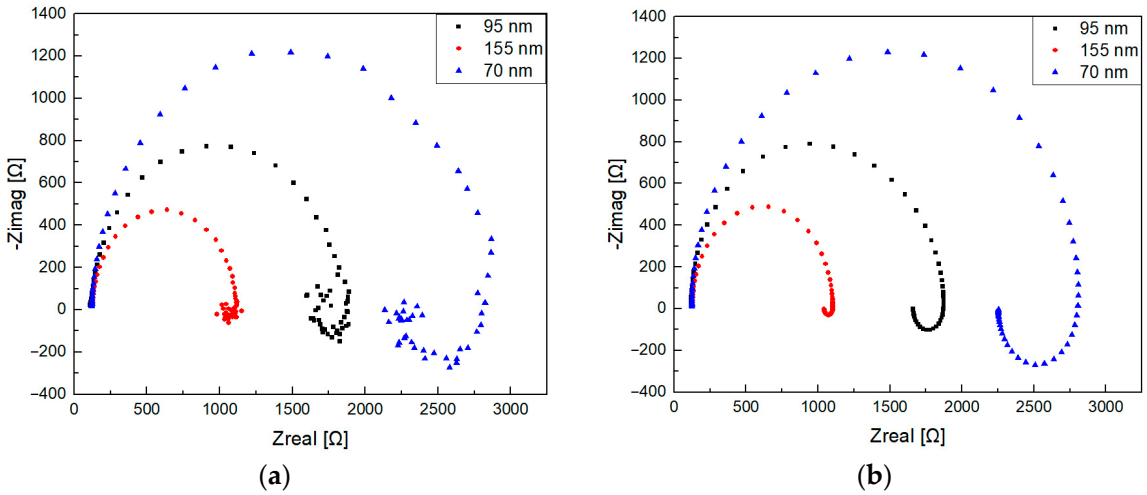

Figure 8. (**a**) The Nyquist plot for the TiO_2-c at 70 nm, 95 nm, and 155 nm thicknesses. (**b**) Equivalent circuit fits for the Nyquist plot for the TiO_2-c at 70 nm, 95 nm, and 155 nm thicknesses.

Table 1 contains the parameters extracted from the equivalent circuit fitting for the varied TiO_2 thickness C-PSCs. The series resistance Rs was the lowest for the 95 nm thickness at 117 Ω, and the highest at 155 nm thickness at 126 Ω.

Table 1. Extracted parameter from the equivalent circuit fitting for varying TiO_2-c thicknesses.

	70 nm	**95 nm**	**155 nm**
R_{HF} (Ω)	2130	1544	916
C_{HF} (F)	1.62×10^{-8}	1.15×10^{-8}	9.24×10^{-9}
L_{LF} (H)	4.044	2.3226	1.3256
R_{series} (Ω)	123	117	126
R_{LF} (Ω)	562.3482	211.8684	70.3789
C_{LF} (F)	8.11×10^{-8}	2.21×10^{-7}	1.86×10^{-7}
τ_{LF} (s)	4.56×10^{-5}	4.67×10^{-5}	1.31×10^{-5}
τ_{HF} (s)	3.44×10^{-5}	1.78×10^{-5}	8.46×10^{-6}

The increase in TiO_2-c thickness is associated with a decrease in the charge transfer resistance from 2130 Ω at 70 nm to 916 Ω at 155 nm. The data suggest that the kinetic barrier for charge transfer at the TiO_2/perovskite is reduced with the increase in the TiO_2-c layer. A decreasing trend is observed for the high-frequency resistance regarding the augmentation of TiO_2-c thickness. Lower R_{ct} values suggest better carrier extraction capabilities [83]. According to the FESEM surface morphology of the TiO_2-c (155 nm), the thicker films were associated with a more uniform, well-crystallized bulk network of mostly circular grains. On the other hand, the FESEM images of the thinner TiO_2-c, such as those of 70 nm and 95 nm, are of a non-uniform network of different grain shapes, with the occurrence of elongated TiO_2 grains more often, which would result in higher R_{ct}.

The C_{LF} is the lowest at the TiO_2-c (70 nm), followed by TiO_2-c (155 nm). The highest C_{LF} is recorded at the 95 nm TiO_2-c thickness. The low-frequency resistance is attributed to the recombination resistance of the carriers. Thinner TiO_2-c PSCs have higher recombination resistance. The relaxation time at the low-frequency arc was found to increase from 45.6 µs at 70 nm to 46.7 µs at 95 nm, then reduce to 13.1 µs for 155 nm.

3.5. Photovoltaic Data

Figure 9 depicts the box plot of the different photovoltaic parameters. A total of 31 PSCs have been fabricated. It can be noticed that the open-circuit voltage (V_{oc}) is the highest in the TiO_2-c thickness range of 95 nm to 115 nm, decreasing for thicknesses outside this range. The short-circuit current (J_{sc}) increases with the TiO_2-c thickness increasing from 70 nm to 135 nm. At 155 nm, the J_{sc} is reduced slightly. The fill factor (FF) exhibits values in the range of 30 to 40 at all TiO_2-c thicknesses. However, the highest FF of 42 was achieved for the 95 nm TiO_2-c thickness, while the lowest value was recorded at the 70 nm layer. The power conversion efficiency (PCE) pattern significantly increases from the 70 nm to 95 nm layer, then continues slightly decreasing as the TiO_2-c thickness increases from 115 nm to 155 nm. In the following paragraphs, the correlation of the TiO_2-c properties with the PSCs' photovoltaic performance will be discussed.

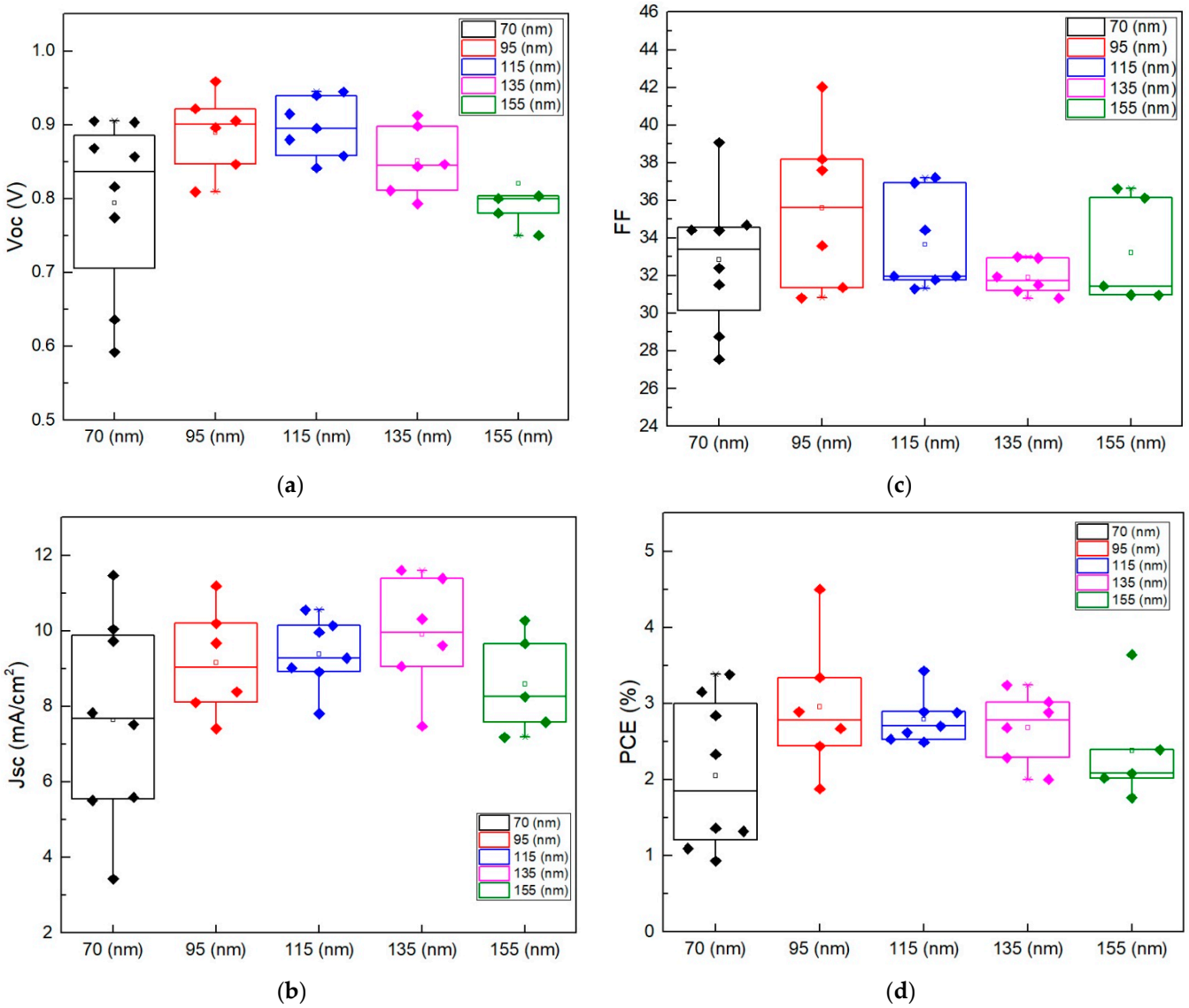

Figure 9. Boxplot of photovoltaic parameters of C-PSCs with variation of TiO_2-c thickness, including (**a**) V_{oc}, (**b**) J_{sc}, (**c**) FF, (**d**) PCE where the black, red, blue, purple, and green filled diamonds represent the individual data points for the 70 nm, 95 nm, 115 nm, 135 nm and 155 nm TiO_2-c thicknesses.

The XRD results showcase the existence of the TiO_2 material in two phases, namely the anatase and the brookite phases. The lowest TiO_2 thickness exhibited higher intensity for the anatase phase in comparison to the brookite phase, followed by the TiO_2-c (95 nm)

displaying an overlap peak intensity between the anatase and brookite peaks. As the thickness is increased, the brookite peak relatively intensifies while that of the anatase phase is reduced, which is more apparent in the TiO_2-c (155 nm) case.

The conduction band of brookite is slightly more cathodic (higher energy) than that of anatase. This allows photo-exited electrons to fall from brookite into anatase, while holes may stay in the brookite side, which ultimately helps in the charge separation. When both brookite and anatase phases exist in TiO_2, electrons and holes are forced into different TiO_2 phases [84].

Md. Shahiduzzaman et al. found that the slightly higher conduction band of brookite (−3.9 eV) than that of anatase (−4.2 eV) creates a favorable energy cascade. The Type-II band alignment allows photo-excited electrons to transfer efficiently from brookite into anatase, while holes are blocked from back transfer, effectively promoting spatial charge separation. When both brookite and anatase coexist in the electron transport layer, this thermodynamic driving force segregates charge carriers, reducing interfacial recombination. It was reported that the heterophane junction can boost the PCE, outperforming the single-phase anatase devices [85].

While the phase evolution is fundamentally driven by thickness-dependent crystallization kinetics during film growth, this structural shift directly dictates the electrical properties of the electron transport layer. The nearly equal XRD peak intensities observed at the 95 nm thickness with a phase ratio of 26 wt% anatase/74 wt% brookite indicate an extensive interfacial area between the anatase and brookite phases. At this specific ratio, the favorable energy cascade from the slightly higher conduction band of brookite into anatase is maximized. This anatase–brookite interaction effectively promotes spatial charge segregation and yields optimal electron extraction compared to films dominated by a single phase. When the thickness is increased, the brookite ratio increases to 81%, minimizing the anatase ratio to 19%, and creating a less favorable energy cascade.

Table 2 illustrates the average and champion photovoltaic parameters for the fabricated PSCs. The increase in short-circuit current density J_{sc} from 7.64 to 9.91 (mA/cm^2) for TiO_2-c thickness between 70 nm and 135 nm can be attributed to the larger aggregates observed from the AFM images. While AFM primarily reflects surface morphology, for thin films in this nanometer regime, laterally larger surface aggregates are indicative of larger crystalline domains extending through the bulk of the film. This has been confirmed by the FESEM results. Thicker TiO_2-c was associated with the nucleation of a well-crystallized continuous bulk network of circular-shaped TiO_2 grains with an average grain size of 70.3 nm. The thin TiO_2-c layer was characterized by a non-continuous network that is filled with a mixture of different sizes and shapes of TiO_2 grains with an average grain size of 60.2 nm. From an electrical standpoint, the larger aggregates associated with thicker TiO_2-c film are highly advantageous. As reported by Jena et al., larger aggregates facilitate superior inter-particle connectivity, creating a robust network for electron percolation. They confirmed that such enhanced physical coalescence minimizes the resistance at grain boundaries, which promotes faster electron transport and correlates directly with improved J_{sc} [86].

However, according to the fitting parameters from the EIS characterization performed, thicker TiO_2-c resulted in reduced R_{rec} for the three characterized cases of 70 nm, 95 nm, and 155 nm. This means that thicker TiO_2-c results in an increasing recombination rate due to the continuous decrease in the recombination resistance. However, a question can arise of why the average J_{sc} increases with the increase of TiO_2-c thickness up to 135 nm. A possible explanation can be suggested from the reduced R_{ct} resistance that is correlated to the increased of TiO_2-c thickness. Lowered charge-transfer resistance results in easier charge extraction at the TiO_2/perovskite interface. The charge extraction mechanism seems

to be outcompeting the recombination mechanisms; therefore, it results in improved J_{sc} up to the thickness where the higher recombination mechanism dominates the dynamics.

Table 2. Photovoltaic parameters of champion cells and the average for varying the TiO_2-c thickness.

		TiO_2-c Thickness				
		70 (nm)	**95 (nm)**	**115 (nm)**	**135 (nm)**	**155 (nm)**
PCE (%)	Champion	3.38	4.5	3.43	3.24	3.64
	Average	2.05 ± 0.99	2.95 ± 0.89	2.79 ± 0.32	2.69 ± 0.47	2.38 ± 0.74
V_{oc} (V)	Champion	0.90	0.96	0.95	0.91	0.97
	Average	0.79 ± 0.12	0.89 ± 0.05	0.90 ± 0.039	0.85 ± 0.04	0.82 ± 0.09
J_{sc} (mA/cm^2)	Champion	11.47	11.19	10.56	11.60	10.27
	Average	7.64 ± 2.70	9.16 ± 1.43	9.38 ± 0.92	9.91 ± 1.54	8.59 ± 1.33
FF	Champion	39.06	42.02	37.20	32.99	36.62
	Average	32.85 ± 3.65	35.60 ± 4.40	33.66 ± 2.54	31.90 ± 0.90	33.23 ± 2.88

In order to isolate the mechanism driving the short-circuit current, the variation in the transmittance spectra for the FTO/TiO_2-c/TiO_2-m reported earlier in the paper was used to estimate the expected theoretical J_{sc}. In order to perform the estimation of J_{sc}, the maximum theoretical photocurrent was calculated by assuming that every photon that passes through the FTO/TiO_2-c/TiO_2-m stack was perfectly absorbed by the $MAPbI_3$ layer and converted into an extracted electron. The following formula was used for the J_{sc} estimation:

$$J_{sc\ expected} = Q \int_{\lambda_{min}}^{\lambda_g} \phi_{AM1.5}(\lambda).T(\lambda)d\lambda$$

where Q is the elementary charge, λ_{min} is the lowest wavelength measured, λ_g is the absorption onset for the perovskite, $\phi_{AM1.5}(\lambda)$ is the AM 1.5G spectral photon flux, and $T(\lambda)$ is the measured transmittance of the FTO/TiO_2-c/TiO_2-m stack.

Table 3 represents the expected J_{sc} calculated from the measured transmittance spectra for different TiO_2-c thicknesses. It can be observed that the expected J_{sc} increases slightly from 21.92 mA/cm^2 at 70 nm to a maximum of 22.82 mA/cm^2 at 115 nm, before reducing to 22.38 mA/cm^2 at the highest thickness of 155 nm. While the actual fabricated PSCs follow a broadly similar trajectory, there are two critical deviations that clarify the dominant performance limitations. First, there is a massive deficit between the expected optical J_{sc} (~22 mA/cm^2) and the actual measured J_{sc} (~7 to 9.9 mA/cm^2), indicating that parasitic photon absorption is not the primary bottleneck. Second, the variation between the highest and lowest expected J_{sc} is only 0.9 mA/cm^2, whereas the actual device J_{sc} varies significantly by 2.27 mA/cm^2.

Table 3. Expected J_{sc} for different TiO_2-c thicknesses for the FTO/TiO_2-c/TiO_2-m stack.

TiO_2-c Thickness (nm)	70 nm	95 nm	115 nm	135 nm	155 nm
Expected J_{sc} (mA/cm^2)	21.92	22.53	22.82	22.57	22.38

Furthermore, while maximum optical transmittance is expected at 115 nm, the actual device J_{sc} continues to increase, peaking at an average of 9.91 mA/cm^2 at 135 nm before sharply reducing to 8.59 mA/cm^2 at 155 nm. This shift demonstrates that increasing the TiO_2-c thickness to 135 nm provides electrical benefits that outweigh the minor reduction

in light transmittance. Consequently, it can be concluded that while optical properties have a marginal effect, the dominant limitations dictating PSC performance at varying TiO_2-c thicknesses are of electrical origin—specifically carrier collection efficiency and interfacial recombination.

The results for the 155 nm film present a trade-off between morphological quality and geometric constraints. The increased path length can also explain the overall device performance reduction. Kotwica et al. demonstrated that thicker electron transport layers introduce higher bulk resistance and probability of recombination. Thus, the increased path length of the 155 nm TiO_2-c layer introduces a greater accumulation of bulk trap states. This increased trap density likely reduces the charge carrier lifetime before extraction, causing the layer to act as a resistive barrier, ultimately lowering the J_{sc} [60]. However, the dominant dynamics that control the J_{sc} at 155 nm in this study are the competition between the fast carrier extraction and higher-recombination mechanisms.

From a different perspective, the reduction in TiO_2-c roughness is associated with a reduction in the subsequent TiO_2-m layer roughness while increasing the thickness of the TiO_2-c layer. The reduction in roughness of the TiO_2-m layer can also be used to explain the higher J_{sc} for the thicker film. It has been reported by Nukunudompanich et al. that the reduction in the TiO_2-c layer roughness reduced the surface area available for nucleation, which in turn promoted lower trap densities within the perovskite layer. They reported that the highest roughness of 9.7 nm achieved with the ethanol solvent resulted in a PCE of 4%, while a reduced surface roughness of 3.9 nm achieved with 1-butanol resulted in a 9% PCE. It should be noted that they were able to achieve a mixed-phase anatase rutile TiO_2 [50].

The highest average V_{oc} was observed for TiO_2-c films within the thickness range of 95 nm to 115 nm, while thicknesses outside this window were associated with lower average V_{oc} values. This behavior likely stems from a combination of structural and optical factors.

First, XRD analysis of the 95 nm film revealed an overlapping of anatase and brookite phase peaks; as noted by Shahiduzzaman et al., such mixed-phase TiO_2 structures are often correlated with higher power conversion efficiencies. Second, optical data confirms that films thinner than 115 nm maintain high transparency (~87%), allowing the maximum light transmission to the perovskite layer. In contrast, the 70 nm films exhibited extreme V_{oc} variation (0.6 V to 0.9 V, average 0.79 V). This instability suggests incomplete surface coverage, where peaks of the FTO substrate may remain exposed or covered only by a permeable, ultra-thin layer, leading to shunting pathways. Conversely, while the thicker films (135 nm to 155 nm) showed less V_{oc} variation, their average voltage decreased. This decline can be attributed to the excessive thickness, which likely increases series resistance, causing charge carriers to accumulate and recombine at the perovskite/TiO_2 interface.

4. Conclusions

The optimization of the compact TiO_2-c layer is a critical factor for the successful ambient-air fabrication of carbon-based perovskite solar cells, particularly in high-humidity environments (RH > 70%). This study demonstrated that TiO_2-c thickness significantly influences the morphological, structural, and photovoltaic properties of the device. Photovoltaic performance was highly sensitive to these structural changes, with the 95 nm thickness identified as the optimal threshold, achieving a peak power conversion efficiency (PCE) of 4.5%. This enhancement is attributed to the synergistic presence of both anatase and brookite phases, larger aggregate formation with improved grain shape uniformity, and reduced surface roughness. In contrast, the lowest performance was recorded at the 70 nm baseline (2.05% average PCE), primarily due to incomplete FTO substrate coverage

and smaller and non-uniform grain sizes, which collectively increase charge trapping and decrease V_{oc} and J_{sc}.

Furthermore, this study reveals a critical trade-off between charge extraction, recombination rate, and transport distance. While increasing the TiO_2-c thickness improves the charge extraction mechanism, both the higher carrier recombination and the increased physical distance ultimately reduce efficiency due to the shorter carrier lifetime. Because 95 nm provided the optimal balance, the results suggest that future optimizations should pair TiO_2-c thickness engineering with perovskite material improvements to extend carrier diffusion lengths. Ultimately, controlling phase composition and surface morphology through precise thickness tuning allows high-performance PSCs to be realized under challenging ambient conditions, providing a clear pathway for low-cost, paintable solar cell production.

Author Contributions: Conceptualization, C.Z.E. and K.-Y.C.; methodology, C.Z.E., P.-L.L., G.S.H.T. and K.-Y.C.; software, C.Z.E. and G.S.H.T.; validation, P.-L.L., Y.-K.S., B.K.Y., K.B.T. and K.-Y.C.; formal analysis, C.Z.E., P.-L.L. and K.-Y.C.; investigation, C.Z.E.; resources, P.-L.L., Y.-K.S. and K.-Y.C.; data curation, C.Z.E.; writing—original draft preparation, C.Z.E.; writing—review and editing, P.-L.L., G.S.H.T., Y.-K.S., B.K.Y., K.B.T. and K.-Y.C.; visualization, G.S.H.T., Y.-K.S., B.K.Y., K.B.T. and K.-Y.C.; supervision, P.-L.L. and K.-Y.C.; project administration, P.-L.L. and K.-Y.C.; funding acquisition, P.-L.L. and K.-Y.C. All authors have read and agreed to the published version of the manuscript.

Funding: The research was funded by the Ministry of Higher Education (MOHE), Malaysia, under the Fundamental Research Grant Scheme (FRGS 2022-1) (Project Ref: FRGS/1/2022/TK08/MMU/03/1).

Data Availability Statement: The data will be provided upon request.

Acknowledgments: We would like to acknowledge the Ministry of Higher Education (MOHE), Malaysia, for the financial support provided under the Fundamental Research Grant Scheme (FRGS 2022-1) (Project Ref: FRGS/1/2022/TK08/MMU/03/1).

Conflicts of Interest: The authors declare no conflicts of interest.

References

1. Sinha, K.K.; Kumar, P.; Gupta, M.K.; Banerjee, M.K. Continuous process of industrial waste water treatment by using solar energy. *SGVU Int. J. Converg. Technol. Manag.* **2022**, *8*, 20–25.
2. Strategic Insight Solar Radiation Resources. In *World Energy Resources: Solar, World Energy Council*; World Energy Council: London, UK, 2013; pp. 1–28.
3. Pourasl, H.H.; Barenji, R.V.; Khojastehnezhad, V.M. Solar energy status in the world: A comprehensive review. *Energy Rep.* **2023**, *10*, 3474–3493. [CrossRef]
4. Maldonado, S. The Importance of New 'Sand-to-Silicon' Processes for the Rapid Future Increase of Photovoltaics. *ACS Energy Lett.* **2020**, *5*, 3628–3632. [CrossRef]
5. Eldjilali, C.Z.; Kah-Yoong, C.; Pei-Ling, L.; How, T.G.S.; Zi-Neng, N.; Ab Rahman, M.; Kar, Y.B. Realization of Perovskite Solar Cells in Ambient Air Environment. *J. Adv. Res. Fluid Mech. Therm. Sci.* **2025**, *130*, 22–33. [CrossRef]
6. Cheng, B.; Xia, X.; Fu, Z.; Jiang, D.; Han, C.; Huo, Y.; Hua, F.; Wang, H.; Cheng, S.; Sun, F.; et al. Achieving 20.9% efficiency organic solar cell enabled by a dual-additive targeted engineering. *Sci. China Chem.* **2026**. [CrossRef]
7. Yeoh, M.-E.; Chan, K.-Y. Recent advances in photo-anode for dye-sensitized solar cells: A review. *Int. J. Energy Res.* **2017**, *41*, 2446–2467. [CrossRef]
8. Yeoh, M.-E.; Chan, K.-Y. A Review on Semitransparent Solar Cells for Real-Life Applications Based on Dye-Sensitized Technology. *IEEE J. Photovoltaics* **2021**, *11*, 354–361. [CrossRef]
9. Acharya, A.; Ye, M.; Kabel, J.; Sharma, S.; Asthana, A.; Neupane, K.; Uddin, J.; Zhang, D.; Yap, Y.K. Efficient Quantum Dot Solar Cells with Sustainable Oxide Thin Films. *ACS Appl. Energy Mater.* **2025**, *8*, 8110–8116. [CrossRef]
10. Kojima, A.; Teshima, K.; Shirai, Y.; Miyasaka, T. Organometal Halide Perovskites as Visible-Light Sensitizers for Photovoltaic Cells. *J. Am. Chem. Soc.* **2009**, *131*, 6050–6051. [CrossRef]
11. Zheng, Y.; Li, Y.; Zhuang, R.; Wu, X.; Tian, C.; Sun, A.; Chen, C.; Guo, Y.; Hua, Y.; Meng, K.; et al. Towards 26% efficiency in inverted perovskite solar cells via interfacial flipped band bending and suppressed deep-level traps. *Energy Environ. Sci.* **2024**, *17*, 1153–1162. [CrossRef]

12. Miah, H.; Khandaker, M.U.; Rahman, B.; Nur-E-Alam, M.; Islam, M.A. Band gap tuning of perovskite solar cells for enhancing the efficiency and stability: Issues and prospects. *RSC Adv.* **2024**, *14*, 15876–15906. [CrossRef]
13. Karunarathne, B.C.; Dunuweera, S.P.; Medagedara, A.T.; Velauthapillai, D.; Punniamoorthy, R.; Perera, A.U.; DeSilva, L.A.; Tennakone, K.; Rajapakse, R.M.G.; Kumara, G.R.A. Low-Cost Perovskite Solar Cell Fabricated using the Expanded Graphite Back Contact and Elec-tronically Conducting Activated Carbon as the Hole Transporting Material. *ACS Omega* **2023**, *8*, 23501–23509. [CrossRef]
14. Arshad, Z.; Shakir, S.; Khoja, A.H.; Javed, A.H.; Anwar, M.; Rehman, A.; Javaid, R.; Qazi, U.Y.; Farrukh, S. Performance Analysis of Calcium-Doped Titania (TiO_2) as an Effective Electron Transport Layer (ETL) for Perovskite Solar Cells. *Energies* **2022**, *15*, 1408. [CrossRef]
15. Uddin, A.; Yi, H. Progress and Challenges of SnO_2 Electron Transport Layer for Perovskite Solar Cells: A Critical Review. *Sol. RRL* **2022**, *6*, 2100983. [CrossRef]
16. Derbali, L.; Bouhjar, F.; Derbali, A.; Soucase, B. Enhanced ZnO-based ETL and nanostructured interface modification for improved perovskite solar cells efficiency. *Opt. Mater.* **2023**, *145*, 114440. [CrossRef]
17. Gong, C.; Li, H.; Xu, Z.; Li, Y.; Wang, H.; Zhuang, Q.; Wang, A.; Li, Z.; Guo, Z.; Zhang, C.; et al. Efficient and stable inverted perovskite solar cells enabled by homogenized PCBM with enhanced electron transport. *Nat. Commun.* **2024**, *15*, 9154. [CrossRef] [PubMed]
18. Liu, X.; Zheng, B.; Shi, L.; Zhou, S.; Xu, J.; Liu, Z.; Yun, J.S.; Choi, E.; Zhang, M.; Lv, Y.; et al. Perovskite solar cells based on spiro-OMeTAD stabilized with an alkylthiol additive. *Nat. Photon.* **2022**, *17*, 96–105. [CrossRef]
19. Wang, Y.; Duan, L.; Zhang, M.; Hameiri, Z.; Liu, X.; Bai, Y.; Hao, X. PTAA as Efficient Hole Transport Materials in Perovskite Solar Cells: A Review. *Sol. RRL* **2022**, *6*, 2200234. [CrossRef]
20. Tang, Z.; Yao, D.; Li, Y.; Li, C.; Xia, T.; Tian, N.; Wang, J.; Zheng, G.; Mo, S.; Long, F.; et al. Efficient and Stable CuSCN-based Perovskite Solar Cells Achieved by Interfacial Engineering with Amidinothiourea. *ACS Appl. Mater. Interfaces* **2024**, *16*, 23973–23984. [CrossRef]
21. Koiry, S.P.; Jha, P.; Sridevi, C.; Gupta, D.; Putta, V.; Chauhan, A.K. Improving perovskite/P3HT interface without an interlayer: Impact of perovskite surface topography on photovoltaic performance of P3HT-based perovskite solar cells. *Mater. Today Commun.* **2023**, *36*, 106418. [CrossRef]
22. Pau, R.; Romero, D.G.; Pitaro, M.; Di Mario, L.; Feng, Q.; Saba, M.; Loi, M.A. Solution-processed CuI as a hole transport layer for Sn–Pb perovskite solar cells. *J. Mater. Chem. A* **2025**, *13*, 42118–42127. [CrossRef]
23. Kang, S.; Zhang, J.; Liang, H.; Huang, J.; Ren, Z.; He, T.; Liu, X.; Zhang, J.; Zhu, Y.; Liu, K.; et al. Water-Soluble V 2 O 5-x Enables Efficient Inverted Perovskite Solar Cells With High Operational and Reverse Bias Stability. *Adv. Energy Mater.* **2025**, *16*, e06005. [CrossRef]
24. Rajbhandari, P.P.; Rijal, B.; Chen, Z.; Choudhary, A.; Efstathiadis, H.; Dhakal, T.P. Performance enhancement of inverted perovskite solar cells through lithium-ion diffusion from the nickel oxide hole transport layer to the perovskite absorber. *Energy Adv.* **2025**, *4*, 1455–1463. [CrossRef]
25. Saliba, M.; Matsui, T.; Domanski, K.; Seo, J.-Y.; Ummadisingu, A.; Zakeeruddin, S.M.; Correa-Baena, J.-P.; Tress, W.R.; Abate, A.; Hagfeldt, A.; et al. Incorporation of rubidium cations into perovskite solar cells improves photovoltaic performance. *Science* **2016**, *354*, 206–209. [CrossRef] [PubMed]
26. Yang, W.S.; Noh, J.H.; Jeon, N.J.; Kim, Y.C.; Ryu, S.; Seo, J.; Seok, S.I. High-performance photovoltaic perovskite layers fabricated through intramolecular exchange. *Science* **2015**, *348*, 1234–1237. [CrossRef]
27. Dong, H.; Pang, S.; Zhang, Y.; Chen, D.; Zhu, W.; Xi, H.; Chang, J.; Zhang, J.; Zhang, C.; Hao, Y. Improving Electron Extraction Ability and Device Stability of Perovskite Solar Cells Using a Compatible PCBM/AZO Electron Transporting Bilayer. *Nanomaterials* **2018**, *8*, 720. [CrossRef]
28. Elseman, A.M. AgSCN as a new hole transporting material for inverted perovskite solar cells. *Sci. Rep.* **2023**, *13*, 7939. [CrossRef]
29. Shao, Y.; Wang, Q.; Dong, Q.; Yuan, Y.; Huang, J. Vacuum-free laminated top electrode with conductive tapes for scalable manufacturing of efficient perovskite solar cells. *Nano Energy* **2015**, *16*, 47–53. [CrossRef]
30. Que, M.; Zhang, B.; Chen, J.; Yin, X.; Yun, S. Carbon-based electrodes for perovskite solar cells. *Mater. Adv.* **2021**, *2*, 5560–5579. [CrossRef]
31. Iqbal, S.; Yin, X.; Wang, B.; Zhang, J.; Nisar, M.Z.; Zhang, J.; Que, W. Fully Printed HTL-Free MAPbI3 Perovskite Solar Cells with Carbon Electrodes. *Coatings* **2023**, *13*, 1338. [CrossRef]
32. Yousaf, T.; Shahzad, N.; Sattar, A.; Tariq, M.A.; Hussain, N.; Khan, Z.S.; Javed, S.; Shahzad, M.I.; Pugliese, D. Performance of Cs-Doped Carbon-Based Perovskite Solar Cells in Ambient Environment. *Energies* **2023**, *16*, 4748. [CrossRef]
33. Verma, A.; Martineau, D.; Abdolhosseinzadeh, S.; Heier, J.; Nüesch, F.A. Inkjet printed mesoscopic perovskite solar cells with custom design capability. *Mater. Adv.* **2020**, *1*, 153–160. [CrossRef]
34. Basit, A.; Rehman, Q.; Noman, M.; Ahmad, M.S.; Wali, Q.; Amir, M.; Khan, A.D. Innovative designs for semitransparent carbon-based perovskite solar cells for building-integrated applications. *Sol. Energy* **2024**, *282*, 112951. [CrossRef]

35. Ryu, J.; Lee, K.; Yun, J.; Yu, H.; Lee, J.; Jang, J. Paintable Carbon-Based Perovskite Solar Cells with Engineered Perovskite/Carbon Interface Using Carbon Nanotubes Dripping Method. *Small* **2017**, *13*, 1701225. [CrossRef]
36. Zhang, H.; Xiao, J.; Shi, J.; Su, H.; Luo, Y.; Li, D.; Wu, H.; Cheng, Y.; Meng, Q. Self-Adhesive Macroporous Carbon Electrodes for Efficient and Stable Perovskite Solar Cells. *Adv. Funct. Mater.* **2018**, *28*, 1802985. [CrossRef]
37. Pashaei, B.; Bellani, S.; Shahroosvand, H.; Bonaccorso, F. Molecularly engineered hole-transport material for low-cost perovskite solar cells. *Chem. Sci.* **2020**, *11*, 2429–2439. [CrossRef]
38. Chen, Y.; Zhang, L.; Zhang, Y.; Gao, H.; Yan, H. Large-area perovskite solar cells—A review of recent progress and issues. *RSC Adv.* **2018**, *8*, 10489–10508. [CrossRef]
39. Wali, Q.; Rabbani, N.A.; Afrin, S.; E Lee, I.; Khan, M.Y. Advances in Electron and Hole Transport Layers-free Perovskite Solar Cells. *Eng. Res. Express* **2026**, *8*, 072301. [CrossRef]
40. Wei, H.; Xiao, J.; Yang, Y.; Lv, S.; Shi, J.; Xu, X.; Dong, J.; Luo, Y.; Li, D.; Meng, Q. Free-standing flexible carbon electrode for highly efficient hole-conductor-free perovskite solar cells. *Carbon* **2015**, *93*, 861–868. [CrossRef]
41. Liu, Z.; Shi, T.; Tang, Z.; Sun, B.; Liao, G. Using a low-temperature carbon electrode for preparing hole-conductor-free perovskite heterojunction solar cells under high relative humidity. *Nanoscale* **2016**, *8*, 7017–7023. [CrossRef]
42. Zhang, L.; Zuo, C.; Zhang, M.; Chen, R.; Chen, X.; Jin, K.; Hao, F.; Yan, K.; Xiao, Z.; Wu, C.; et al. Antisolvent-Bathing Strategy with Ultra-Wide Processing Window for Making High-efficiency Perovskite Solar Cells in Ambient Air. *Angew. Chem. Int. Ed. Engl.* **2025**, *64*, e202506418. [CrossRef] [PubMed]
43. Tai, Q.; You, P.; Sang, H.; Liu, Z.; Hu, C.; Chan, H.L.W.; Yan, F. Efficient and stable perovskite solar cells prepared in ambient air irrespective of the humidity. *Nat. Commun.* **2016**, *7*, 11105. [CrossRef]
44. Masood, M.T.; Weinberger, C.; Sarfraz, J.; Rosqvist, E.; Sandén, S.; Sandberg, O.J.; Vivo, P.; Hashmi, G.; Lund, P.D.; Österbacka, R.; et al. Impact of Film Thickness of Ultrathin Dip-Coated Compact TiO_2 Layers on the Performance of Mesoscopic Perovskite Solar Cells. *ACS Appl. Mater. Interfaces* **2017**, *9*, 17906–17913. [CrossRef]
45. Miao, S.; Yuan, S.; Zhu, D.; Cai, Q.; Wang, H.-Y.; Wang, Y.; Qin, Y.; Ai, X.-C. Mesoporous TiO 2 layer suppresses ion accumulation in perovskite solar cells. *Phys. Chem. Chem. Phys.* **2022**, *24*, 20689–20693. [CrossRef]
46. Hayali, A.; Alkaisi, M.M. High efficiency perovskite solar cells using DC sputtered compact TiO_2 electron transport layer. *EPJ Photovoltaics* **2021**, *12*, 8. [CrossRef]
47. Pylnev, M.; Santos, F.R.; Zhang, D.; Alawadhi, H.; Tabet, N. Compact TiO_2 layer by UV-assisted TiBr4 chemical bath deposition for perovskite solar cells. *Mater. Sci. Semicond. Process.* **2023**, *161*, 107467. [CrossRef]
48. Bracesco, A.E.A.; Burgess, C.H.; Todinova, A.; Zardetto, V.; Koushik, D.; Kessels, W.M.M.; Dogan, I.; Weijtens, C.H.L.; Veenstra, S.; Andriessen, R.; et al. The chemistry and energetics of the interface between metal halide perovskite and atomic layer deposited metal oxides. *J. Vac. Sci. Technol. A* **2020**, *38*, 063206. [CrossRef]
49. Kumar, S.; Aftab, A.; Ahmad, I. Compact Titania Films by Spray Pyrolysis for Application as ETL in Perovskite Solar Cells. *J. Electron. Mater.* **2020**, *49*, 7159–7167. [CrossRef]
50. Nukunudompanich, M.; Suzuki, K.; Kameda, K.; Manzhos, S.; Ihara, M. Nano-scale smooth surface of the compact-TiO_2 layer via spray pyrolysis for controlling the grain size of the perovskite layer in perovskite solar cells. *RSC Adv.* **2023**, *13*, 27686–27695. [CrossRef] [PubMed]
51. Zhang, H.; Wang, H.; Ma, M.; Wu, Y.; Dong, S.; Xu, Q. Application of Compact TiO_2 Layer Fabricated by Pulsed Laser Deposition in Organometal Trihalide Perovskite Solar Cells. *Sol. RRL* **2018**, *2*, 1800097. [CrossRef]
52. Tseng, Y.-T.; Tseng, Y.-T.; Wu, C.-C. Photovoltaic Performance of CH3NH3PbI2Cl Perovskite Solar Cell. *Appl. Funct. Mater.* **2022**, *2*, 14–20. [CrossRef]
53. Wu, J.; Wang, Y.; Su, C.; Zhou, H.; Xu, H.; Jin, L. Preparation and characterization of planar heterojunction perovskite solar cells based on c-TiO2/CH3NH3PbI3/HTM/Ag structure. *J. Sol-Gel Sci. Technol.* **2021**, *100*, 440–450. [CrossRef]
54. Huang, P.-H.; Huang, C.-W.; Kang, C.-C.; Hsu, C.-H.; Lien, S.-Y.; Wang, N.-F.; Huang, C.-J. The Investigation for Coating Method of Titanium Dioxide Layer in Perovskite Solar Cells. *Crystals* **2020**, *10*, 236. [CrossRef]
55. Sassi, S.; Bouich, A.; Hajjaji, A.; Khezami, L.; Bessais, B.; Soucase, B.M. Cu-Doped TiO_2 Thin Films by Spin Coating: Investigation of Structural and Optical Properties. *Inorganics* **2024**, *12*, 188. [CrossRef]
56. Veiga, E.T.; Fernandes, S.L.; Graeff, C.F.d.O.; Polo, A.S. Compact TiO_2 blocking-layer prepared by LbL for perovskite solar cells. *Sol. Energy* **2021**, *214*, 510–516. [CrossRef]
57. Gouda, L.; Rietwyk, K.J.; Hu, J.; Kama, A.; Ginsburg, A.; Priel, M.; Keller, D.A.; Tirosh, S.; Meir, S.; Gottesman, R.; et al. High-Resolution Study of TiO_2 Contact Layer Thickness on the Performance of Over 800 Perovskite Solar Cells. *ACS Energy Lett.* **2017**, *2*, 2356–2361. [CrossRef]
58. Liu, H.; Bala, H.; Zhang, B.; Zong, B.; Huang, L.; Fu, W.; Sun, G.; Cao, J.; Zhan, Z. Thickness-dependent photovoltaic performance of TiO_2 blocking layer for perovskite solar cells. *J. Alloy. Compd.* **2018**, *736*, 87–92. [CrossRef]
59. Sun, W.; Choy, K.-L.; Wang, M. The Role of Thickness Control and Interface Modification in Assembling Efficient Planar Perovskite Solar Cells. *Molecules* **2019**, *24*, 3466. [CrossRef] [PubMed]

60. Sławek, A.; Starowicz, Z.; Lipiński, M. The Influence of the Thickness of Compact TiO2 Electron Transport Layer on the Performance of Planar CH3NH3PbI3 Perovskite Solar Cells. *Materials* **2021**, *14*, 3295. [CrossRef]
61. Elshimy, H.; Abdallah, T.; Shama, A.A. Optimization of Spin Coated TiO_2 Layer for Hole-Free Perovskite Solar Cell. *IOP Conf. Ser. Mater. Sci. Eng.* **2020**, *762*, 012003. [CrossRef]
62. Zhang, C.; Luo, Y.; Chen, X.; Ou-Yang, W.; Chen, Y.; Sun, Z.; Huang, S. Influence of different TiO_2 blocking films on the photovoltaic performance of perovskite solar cells. *Appl. Surf. Sci.* **2016**, *388*, 82–88. [CrossRef]
63. Meyerhofer, D. Characteristics of resist films produced by spinning. *J. Appl. Phys.* **1978**, *49*, 3993–3997. [CrossRef]
64. Liu, H.; Fu, X.; Fu, W.; Zong, B.; Huang, L.; Bala, H.; Wang, S.; Guo, Z.; Sun, G.; Cao, J.; et al. An effective TiO_2 blocking layer for hole-conductor-free perovskite solar cells based on carbon counter electrode. *Org. Electron.* **2018**, *59*, 253–259. [CrossRef]
65. Gong, X.-Q.; Selloni, A. First-principles study of the structures and energetics of stoichiometric brookite TiO_2 surfaces. *Phys. Rev. B* **2007**, *76*, 235307. [CrossRef]
66. Du, Y.; Niu, X.; Li, W.; Liu, J.; Li, J. Synthesis of High-Energy Faceted TiO_2 Nanocrystals with Enhanced Photocatalytic Performance for the Removal of Methyl Orange. *Catalysts* **2022**, *12*, 1534. [CrossRef]
67. Kandiel, T.A.; Robben, L.; Alkaima, A.; Bahnemann, D. Brookite versus anatase TiO_2 photocatalysts: Phase transformations and photocatalytic activities. *Photochem. Photobiol. Sci.* **2012**, *12*, 602–609. [CrossRef] [PubMed]
68. Wang, Y.; Feng, T.; Li, X.; Li, L. Thermochemistry of nano-phased titanium dioxides relevant to energy application: A Review. *Chem. Thermodyn. Therm. Anal.* **2022**, *5*, 100033. [CrossRef]
69. Balagowtham, N.; Acchutharaman, K.R.; Santhosh, N.; Pandian, M.S.; Ramasamy, P. Highly stable MAPbI3 microcrystals: A single precursor derived from low-grade PbI2 using sono-chemical method for economical and efficient perovskite solar cells. *J. Mater. Sci. Mater. Electron.* **2022**, *33*, 21531–21545. [CrossRef]
70. Eldjilali, C.Z.; Thien, G.S.H.; Ng, Z.-N.; Yap, B.K.; Tan, K.B.; Murthy, H.A.; Chan, K.-Y. Electrochromic performances of TiO_2 nanocrystals thin films for smart glass applications. *Thin Solid Films* **2025**, *815*, 140636. [CrossRef]
71. Gohari, G.; Mohammadi, A.; Akbari, A.; Panahirad, S.; Dadpour, M.R.; Fotopoulos, V.; Kimura, S. Titanium dioxide nanoparticles (TiO_2 NPs) promote growth and ameliorate salinity stress effects on essential oil profile and biochemical attributes of Dracocephalum moldavica. *Sci. Rep.* **2020**, *10*, 912. [CrossRef] [PubMed]
72. Arunmetha, S.; Dhineshbabu, N.R.; Kumar, A.; Jayavel, R. Preparation of sulfur doped TiO_2 nanoparticles from rutile sand and their performance testing in hybrid solar cells. *J. Mater. Sci. Mater. Electron.* **2021**, *32*, 28382–28393. [CrossRef]
73. Al-Oubidy, E.A.; Kadhim, F.J. Photocatalytic activity of anatase titanium dioxide nanostructures prepared by reactive magnetron sputtering technique. *Opt. Quantum Electron.* **2019**, *51*, 23. [CrossRef]
74. Mishra, A.; Ahmad, Z.; Touati, F.; Shakoor, R.A.; Nazeeruddin, M.K. One-dimensional facile growth of MAPbI 3 perovskite micro-rods. *RSC Adv.* **2019**, *9*, 11589–11594. [CrossRef] [PubMed]
75. Sivakumar, N.; Saha, S.; Madaka, R.; Bandaru, N.; Rath, J.K. Investigation on the structural, spectral, and optical properties of MAPbI3.H_2O and MAPbI3 perovskite crystals for photovoltaic cells. *J. Mater. Sci. Mater. Electron.* **2023**, *34*, 1193. [CrossRef]
76. Cadatal-Raduban, M.; Pope, J.; Olejníček, J.; Kohout, M.; Harrison, J.A.; Hasan, S.M.R. Ultraviolet-C Photoresponsivity Using Fabricated TiO_2 Thin Films and Transimpedance-Amplifier-Based Test Setup. *Sensors* **2022**, *22*, 8176. [CrossRef]
77. Dundar, I.; Mere, A.; Mikli, V.; Krunks, M.; Acik, I.O. Thickness Effect on Photocatalytic Activity of TiO_2 Thin Films Fabricated by Ultrasonic Spray Pyrolysis. *Catalysts* **2020**, *10*, 1058. [CrossRef]
78. Chen, W.; Koshy, P.; Zhu, B.; Sorrell, C. Effect of Film thickness on the Photocatalytic Performance of TiO_2 Thin Films Deposited by Spin Coating. In *Ceramic Materials for Energy Applications IV*; American Ceramic Society: Hoboken, NJ, USA, 2014; Volume 35, pp. 51–60. [CrossRef]
79. Huang, A.; Zhu, J.; Zhou, Y.; Yu, Y.; Liu, Y.; Yang, S.; Ji, S.; Lei, L.; Jin, P. One step spray-coated TiO_2 electron-transport layers for decent perovskite solar cells on large and flexible substrates. *Nanotechnology* **2016**, *28*, 01LT02. [CrossRef] [PubMed]
80. Clarke, W.; Richardson, G.; Cameron, P. Understanding the Full Zoo of Perovskite Solar Cell Impedance Spectra with the Standard Drift-Diffusion Model. *Adv. Energy Mater.* **2024**, *14*, 2400955. [CrossRef]
81. Neupane, G.R.; Bamidele, M.; Yeddu, V.; Kim, D.Y.; Hari, P. Negative capacitance and hysteresis in encapsulated MAPbI3 and lead–tin (Pb–Sn) perovskite solar cells. *J. Mater. Res.* **2022**, *37*, 1357–1372. [CrossRef]
82. Fabregat-Santiago, F.; Kulbak, M.; Zohar, A.; Vallés-Pelarda, M.; Hodes, G.; Cahen, D.; Mora-Seró, I. Deleterious Effect of Negative Capacitance on the Performance of Halide Perovskite Solar Cells. *ACS Energy Lett.* **2017**, *2*, 2007–2013. [CrossRef]
83. Bulowski, W.; Szwanda, A.; Gawlińska-Nęcek, K.; Panek, P.; Lipiński, M.; Janusz-Skuza, M.; Szczerba, M.J.; Majchrowicz, Ł.; Mahapatra, A.; Prochowicz, D.; et al. Optimization of the ETL titanium dioxide layer for inorganic perovskite solar cells. *J. Mater. Sci.* **2024**, *59*, 7283–7298. [CrossRef]
84. Tay, Q.; Liu, X.; Tang, Y.; Jiang, Z.; Sum, T.C.; Chen, Z. Enhanced Photocatalytic Hydrogen Production with Synergistic Two-Phase Anatase/Brookite TiO_2 Nanostructures. *J. Phys. Chem. C* **2013**, *117*, 14973–14982. [CrossRef]

85. Shahiduzzaman; Visal, S.; Kuniyoshi, M.; Kaneko, T.; Umezu, S.; Katsumata, T.; Iwamori, S.; Kakihana, M.; Taima, T.; Isomura, M.; et al. Low-Temperature-Processed Brookite-Based TiO_2 Heterophase Junction Enhances Performance of Planar Perovskite Solar Cells. *Nano Lett.* **2018**, *19*, 598–604. [CrossRef]
86. Jena, A.K.; Mohanty, S.P.; Bhargava, P. Effect of Sintering Profiles on Titania Interparticle Connectivity, Electron Transport and Interfacial Resistance in Dye-Sensitized Solar Cells. *Mater. Sci. Forum* **2013**, *771*, 143–157. [CrossRef]